ORNL/TM-2021/2308

Oak Ridge National Laboratory Seismo-acoustic Characteristics of HFIR Cooling Tower Fans and Pumps

Chengping Chai
Monica Maceira
Omar Marcillo

September 2021

OAK RIDGE National Laboratory

ORNL IS MANAGED BY UT-BATTELLE LLC FOR THE US DEPARTMENT OF ENERGY

ORNL/TM-2021/2308

Nuclear Nonproliferation Division

SEISMO-ACOUSTIC CHARACTERISTICS OF HFIR COOLING TOWER FANS AND PUMPS

Author(s)

Chengping Chai
Monica Maceira
Omar Marcillo

September 2021

Prepared by
OAK RIDGE NATIONAL LABORATORY
Oak Ridge, TN 37831-6283
managed by
UT-BATTELLE LLC
for the
US DEPARTMENT OF ENERGY
under contract DE-AC05-00OR22725

CONTENTS

LIST OF FIGURES

ABSTRACT

Seismic and acoustic characteristics of three cooling tower pumps and four fans at High Flux Isotope Reactor (HFIR) were investigated using data from three targeted experiments on December 6, 2019, June 5, 2020, and February 10–11, 2021. We used spectrograms, power spectral density (PSD), an interactive frequency picking tool, and ground truth information to study seismic and acoustic responses due to the operating of these pumps and fans. By varying operating speed of the fans, we found faster fan speed leads to higher seismic and acoustic energy. A stepwise increase in fan speed leads to a station-specific stepwise pattern in seismic spectrograms. At each fan speed and for each fan, different impulsive frequencies can be identified using the interactive frequency picker. Seismic responses of two fans operating concurrently are equivalent to the summation of seismic responses of each fan. We can match the acoustic response of fans from one targeted experiment with that from three actual operational cycles of HFIR. Seismic responses of the fans show significant differences at different stations even for the same fan operating at the same speed, though common impulsive frequencies can be found in most cases. Unlike the fans, seismic responses of the cooling tower pumps contain mostly broadband features in the frequency band of 5–50 Hz (or 5–150 Hz for some stations). Clear seismic responses of the three cooling tower pumps were observed at all seismic stations with a maximum distance of 120 m. As expected, seismic energy is higher when the sensor is located closer to the source. We were able to locate the source of pump-related seismic responses using absolute amplitudes of seismic signals. The inferred source location region includes the actual location of the pump, which may be improved with a polarization analysis of seismic signals.

1. INTRUDOCUTION

Seismic and acoustic sensors can detect ground motions and pressure waves due to industrial operations (e.g., Snow 1997; Marcillo and MacCarthy 2020; Guenaga et al. 2021). For nuclear reactors, seismo-acoustic signals provide an opportunity to monitor industrial operations (Marcillo et al. 2021). Marcillo et al. (2021) identified a correlation between seismo-acoustic energy and the main power of the High Flux Isotope Reactor (HFIR) at Oak Ridge National Laboratory (ORNL). Guenaga et al. (2021) used a PSD detector and identified at least 19 unique operations from 11 months of seismic data. However, the seismic and acoustic characteristics of individual machines have not been thoroughly investigated.

HFIR's cooling tower plays a critical role in maintaining the reactor's temperature to a safe level. Operations of the cooling tower generate large-amplitude seismic and acoustic signals. Multiple machines of the cooling tower including four fans and three pumps operate systematically to ensure the coolant maintains the designed temperature. The four fans are located on the top of the cooling tower, and the three pumps are located on the west side of the tower (Figure 1). To investigate the seismic and acoustic characteristics of the fans and pumps of the cooling tower, we carried out three targeted data collections on December 6, 2019, June 5, 2020, and February 10–11, 2021. Spectrograms, PSDs, and source location analysis were used to extract useful information from collected seismo-acoustic data. An interactive tool was also developed to support lightweight data processing and visualization in a browser.

Figure 1. A satellite image from Google Earth showing locations of seismic sensors with respect to HFIR at ORNL in Oak Ridge, Tennessee, USA. WACO is a permanent seismo-acoustic station. The orange symbols indicate a temporary deployment. A, B, C and D indicate the four fans of the cooling tower. SA, SB, and SC denote three pumps attached to the cooling tower.

2. DATA

2.1 FAN TEST ON DECEMBER 6, 2019, AND JUNE 5, 2020

We used seismic and acoustic data recorded at a seismo-acoustic station WACO for two fan tests on December 6, 2019, and June 5, 2020. The station is located about 50 m from the HFIR cooling tower. A three-component 4.5 Hz GeoSpace geophone and three Inter-Mountain Labs infrasound sensors were deployed at the station. The station also includes a Reftek digitizer and GPS time synchronization. Both seismic and acoustic sensors have a sampling rate of 500 Hz. During the fan tests, the four fans (Fan A, B, C, and D) on top of the cooling tower were configured to operate at different speeds. Fan A and B can operate at 50% or 100% speed, but the speed of Fan C and D can vary continuously. Ground truth information on the time and speed of each of the four fans were recorded. During the December 6, 2019, fan test, the four cooling tower fans were configured to operate individually at different speeds. During the June 5, 2020, fan test, two fans were operating simultaneously.

2.2 FAN TEST ON FEBRUARY 20, 2021, AND PUMP TEST ON FEBRUARY 11, 2021

We deployed 24 temporary 3-component seismic sensors around the HFIR cooling tower (Figure 1) for a fan test on February 10, 2021, and a pump test on February 11, 2021. Because of site condition restrictions (e.g., paved surface and steep slope), most (18) sensors were deployed on the south of the cooling tower. The furthest station located about 120 m from the center of the cooling tower. These sensors have a sampling rate of 2,000 Hz. Acoustic sensors were not available during this temporary deployment. Similar to the other two fan tests, the four cooling tower fans were configured to operate at different speeds. During the pump test, three secondary cooling pumps (SA, SB, and SC) and two pool cooling pumps (PA and PB, located in HFIR main building) were arranged to operate individually for around 10 min. Ground truth data for fan speeds and pump operational states were available.

3. METHOD

3.1 SPECTROGRAM

To obtain an overall view of the data associated with the fan and pump tests, we first compute and plot the spectrogram of both seismic and acoustic channels. The spectrogram was computed using a Fourier transform over 10 s time windows with a 50% overlap. Ground truth information from the fan tests or pump test were displayed with the spectrogram to identify correlations between the two.

3.2 POWER SPECTRAL DENSITY

We used PSDs to further investigate the frequencies related to each fan and at various speeds. Specifically, we compute PSDs using 10 s time windows with a 50% overlap for each time segment that fans or pumps have the same operational states. The PSDs were then averaged in each time segment to reduce noise. To remove long (days) operational events and background noise, we subtracted background responses from the data related to fans and pumps. The background responses were computed by averaging PSDs in a time window right before or after a fan or pump test. We examined the resulting background-removed PSDs corresponding to each fan and at each tested speed for both seismic and acoustic data. We also subtracted one PSD from another PSD to investigate signal superposition when two fans were operating concurrently. PSDs from the fan test was also compared against PSDs associated with normal HFIR operating cycles.

3.3 INTERACTIVE TOOL

To measure frequencies related to fans or pumps from PSDs more efficiently, we developed an interactive tool similar to the applications by Chai et al. (2018). Figure 2 is a screenshot of the interactive tool. The tool uses a modern browser interface for lightweight data processing and visualization. A PSD curve from a text file stored in comma-separated values (CSV) format can be imported by clicking a button. The CSV file contains two columns: frequency and amplitude. After the file is loaded, the PSD curve will be displayed in an interactive panel. The user can click on or adjacent to a data point to select it as point of interest. The selected data points are marked as red dots with corresponding values listed in a table below. The panel also allows a user to choose or delete a previously selected data point and zoom-in for a more detailed view. Once the selection process is complete, the selected values can be saved to a CSV file with one click.

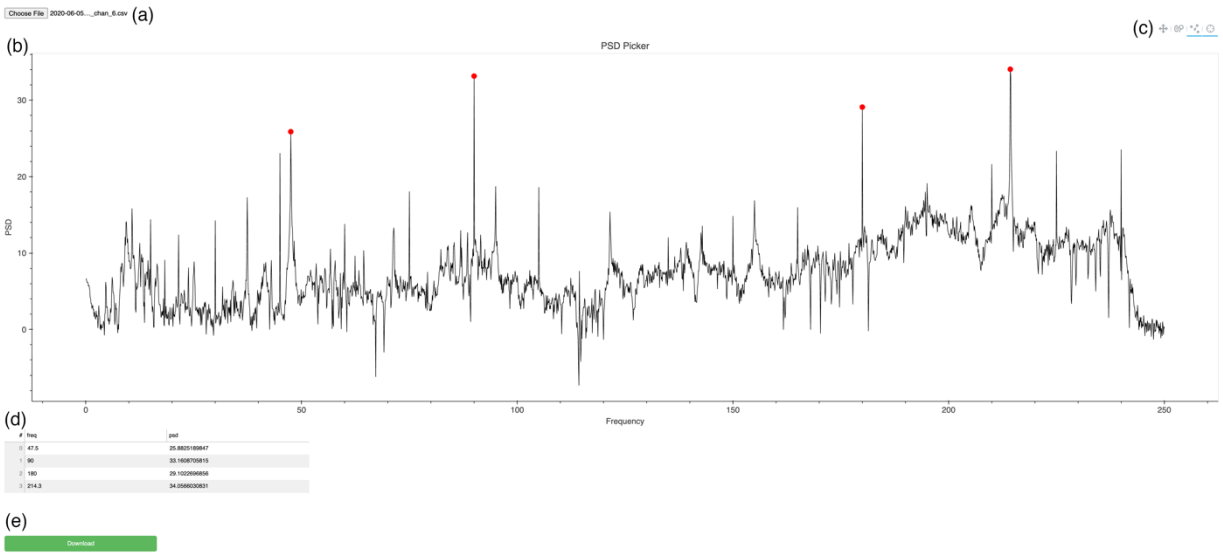

Figure 2. A screenshot of the PSD frequency picker. (a) A button to import PSD data from a text file. (b) An interactive panel that displays the PSD curve and allows a user to select points of interest. (c) Interactive tools, including a zoom option. (d) A table that lists data points selected. (e) A button to save the selected data points to a text file.

3.4 SOURCE LOCATION

We used absolute amplitudes of seismic data recorded at the 24 temporary stations to obtain the geolocation of a specific mechanical source. Traditional source location uses travel times between the source and receivers. The short (tens of meters to a hundred meters) source-to-receiver distance requires us to measure the travel times within an accuracy of a few samples to produce a meaningful location. As the recorded seismic signals related to fans and pumps are not impulsive, we cannot measure the arrival times of these signals accurately enough for a travel time–based location analysis. However, the absolute amplitude of these seismic signals associated with the fan and pump tests shows clear spatial variations. The amplitude variation can be calculated if we know the location of the source. We carried out a grid search to find the location of a source. Specifically, we divided the study area into a 1 m × 1 m evenly spaced grid. At each grid point, we computed the theoretical amplitude at each seismic station assuming the source is located at the grid point. A root mean square (RMS) error for the grid point was then calculated with the observed and modeled amplitudes. The minimum RMS errors of the entire grid indicate where the source was likely located.

4. RESULTS

4.1 SPECTROGRAM

Figure 3 and Figure 4 show the recorded signals and their spectrograms of the seismic and acoustic data for the December 6, 2019, fan test. We see a clear increase in energy (square sum of amplitude) for both seismic and acoustic data when a fan is operating at a speed faster than 50%. The correlation between the fast (lager than 50%) fan speed and the seismo-acoustic data is more obvious on spectrograms. The seismic spectrogram also shows patterns (around 10:30 and 11:00) that are not recorded by acoustic sensors and do not relate to ground truth information. These patterns are likely caused operational events that generate ground motions but not observable acoustic energy. For fan speed faster than 50%, higher

fan speed leads to higher seismic and acoustic energy (larger amplitude in Figure 3a and Figure 4a or warmer colors in Figure 3c and Figure 4c). A different series of frequencies were illuminated on the acoustic spectrogram (Figure 4c) for different fan speeds. Comparing spectrogram segments for different fans with the same speed, we see noticeable differences.

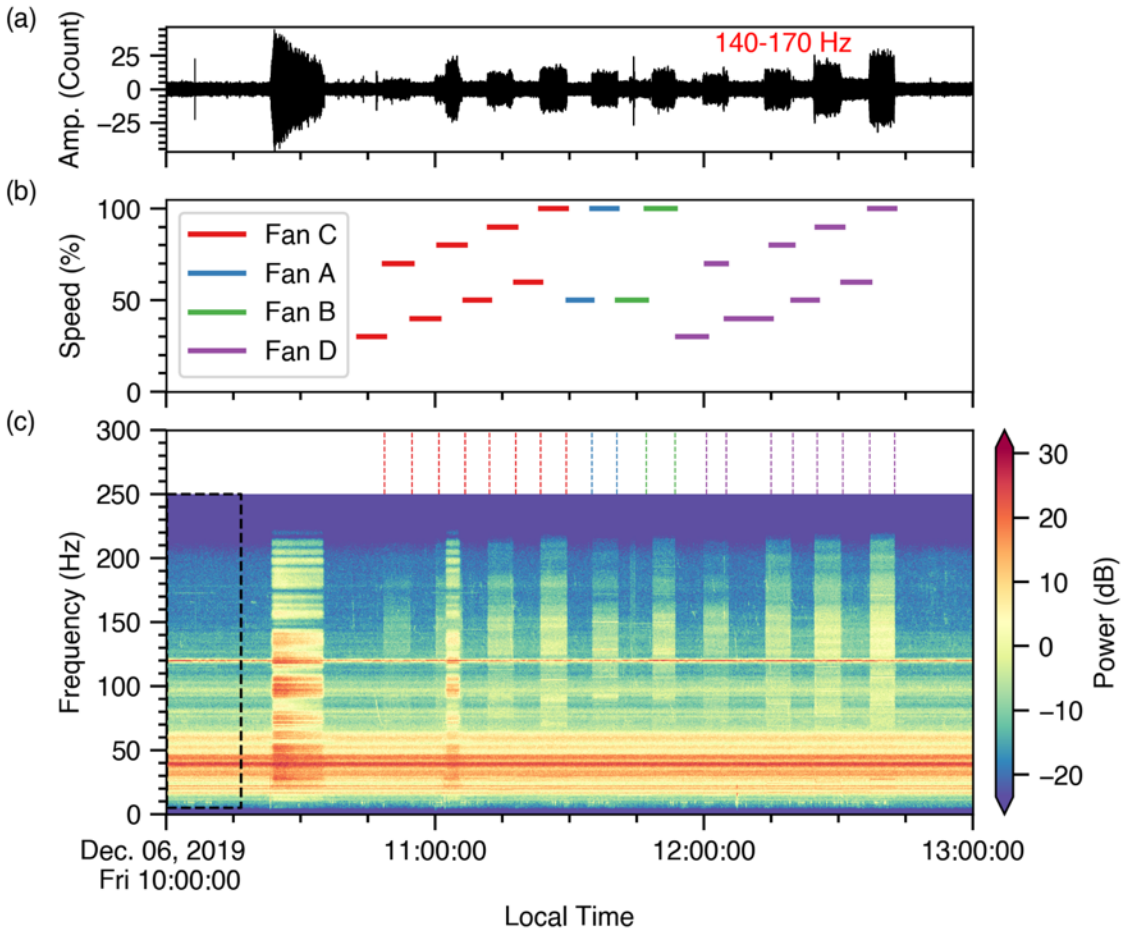

Figure 3. Seismic data recorded at WACO during the fan test on December 6, 2019. Panel (a) shows the vertical-component seismogram filtered with a bandpass filter between 140 and 170 Hz. Panel (b) shows the ground truth fan speed. Panel (c) shows the spectrogram of the seismic data. The dashed vertical lines indicate when fan speed changes were occurred. The dashed box shows the time window that was used as background.

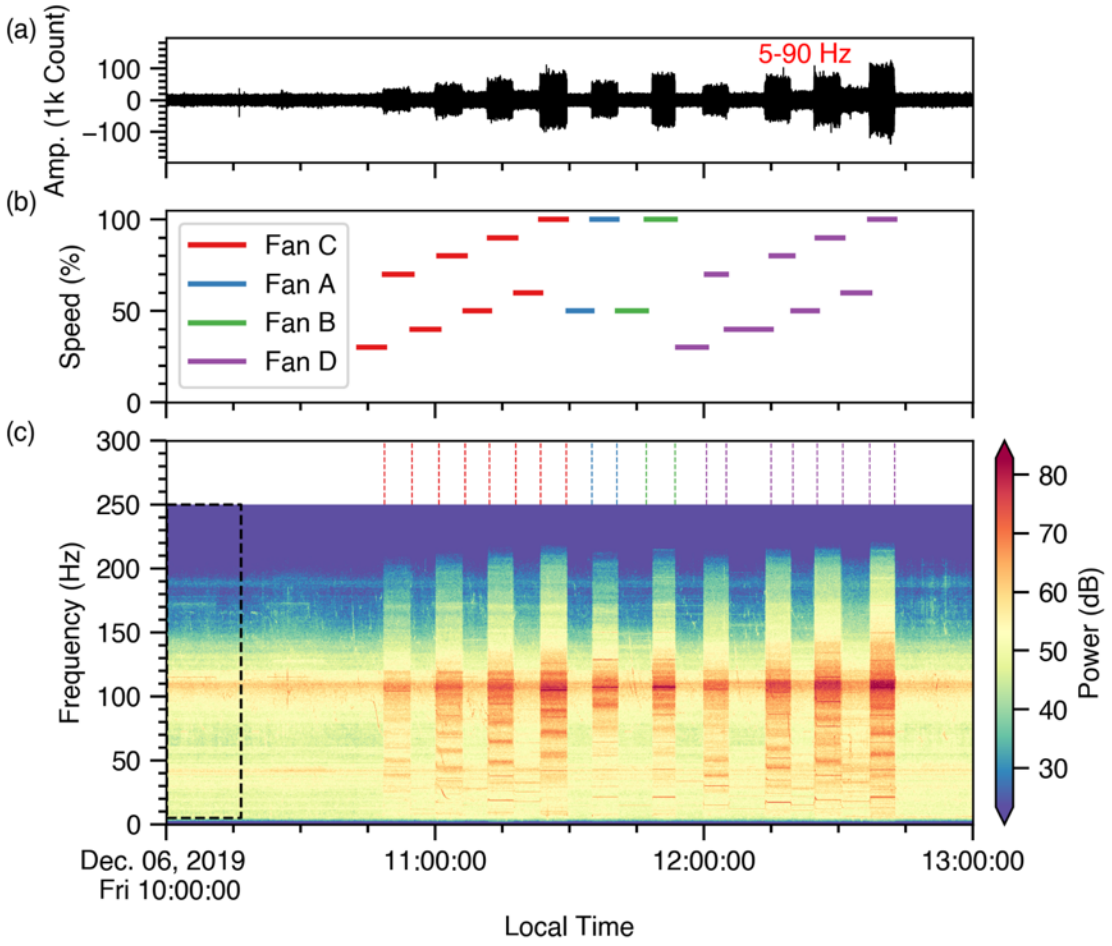

Figure 4. Acoustic data recorded at WACO during the fan test on December 6, 2019. Panel (a) shows the acoustic data filtered with a bandpass filter between 5 and 90 Hz. Panel (b) shows the ground truth fan speed. Panel (c) shows the spectrogram of the acoustic data. The dashed vertical lines in panel (c) indicate when fan speed changes were occurred. The dashed box shows the time window that was used as background.

The seismic and acoustic data and their spectrogram for the June 5, 2020, fan test are shown in Figure 5 and Figure 6. In addition to patterns similar to those for the December 6, 2019, fan test, we found that the seismic and acoustic responses of two fans operating together includes features corresponding to each fan operating individually. Patterns that do not relate to the ground truth information around 12:45 and 13:00 (local time) were recorded by both seismic and acoustic sensors (Figure 5c and Figure 6c). These patterns are likely associated with operational events that generate ground motions and emit acoustic energy.

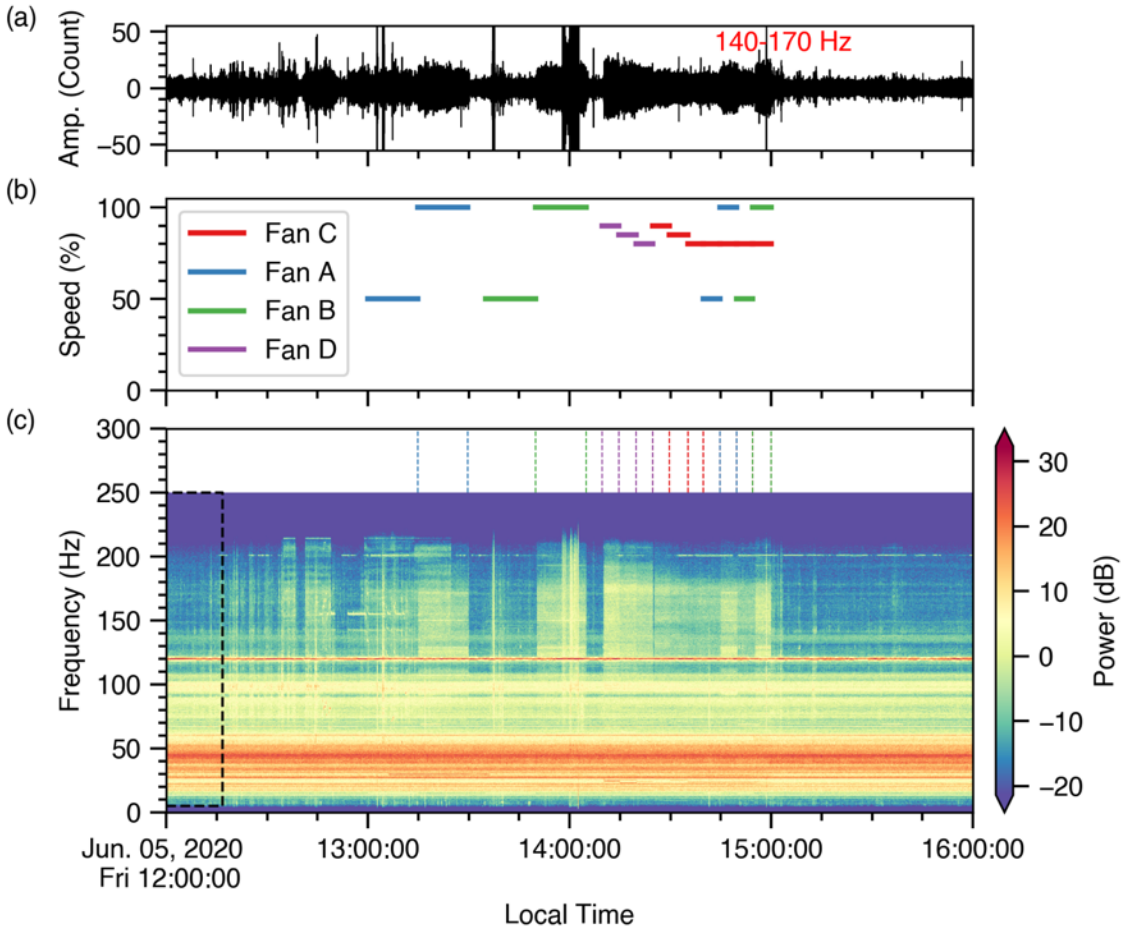

Figure 5. Seismic data recorded at WACO the fan test on June 5, 2020. The figure layout and symbols are the same as Figure 3.

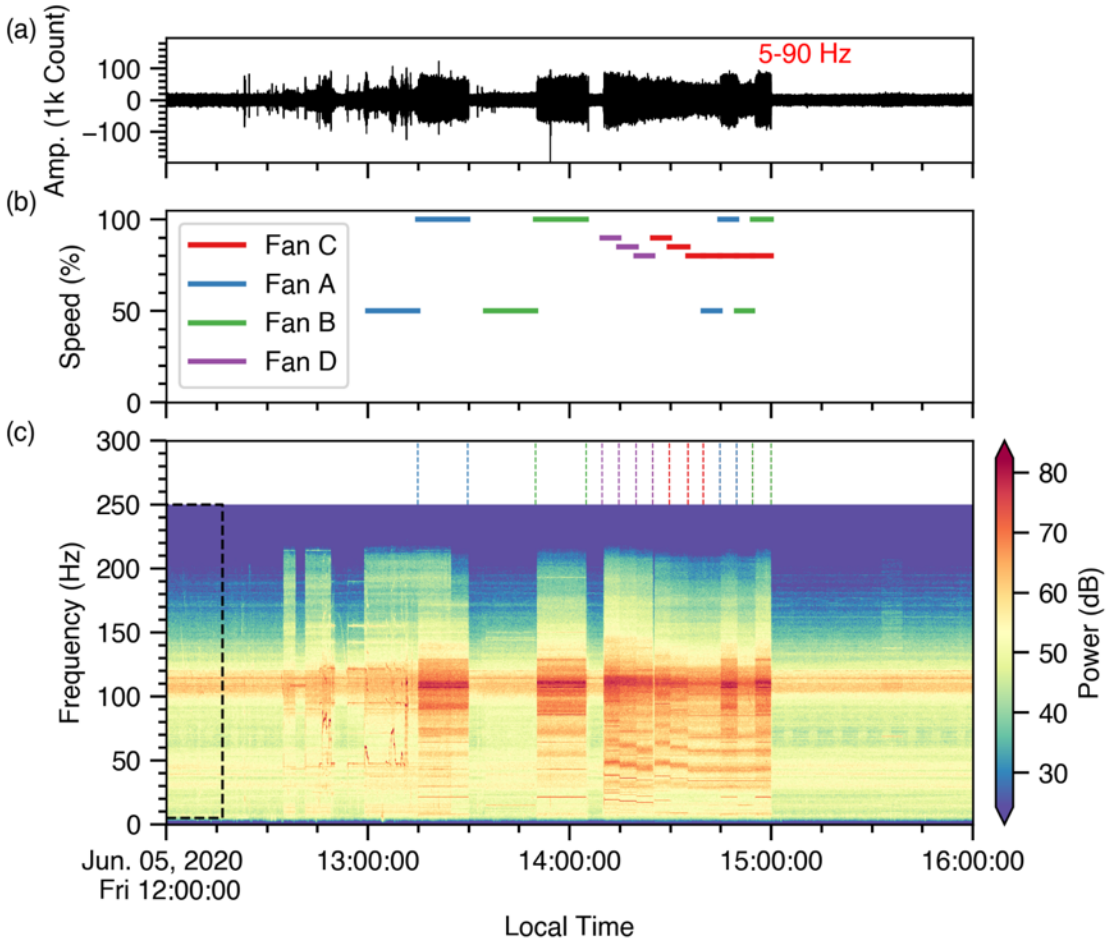

Figure 6. Acoustic data recorded at WACO for the fan test on June 5, 2020. The figure layout and symbols are the same as Figure 4.

The temporary seismic array deployed for the February 10, 2021, fan test and February 11, 2021, pump test allows us to explore the spatial variation of the seismic wavefield. All the stations recorded clear seismic responses from both the fans and the secondary cooling pumps (pump SA, SB, and SC). The seismic data do not show responses from the pumps located in the main building of HFIR (pump PA and PB). We focus our analysis on one station (264128) located to the north and one station (264114) located in the southwest of the cooling tower with distances of 45 m and 104 m from the center of the tower, respectively. We can see higher seismic power correlates with faster fan speeds at both stations (Figure 7 and Figure 8). The response of two fans operating concurrently contains signatures from the two individual fans. The stepwise increases in fan speed for fans C and D led to stepwise patterns in the seismic spectrogram at both stations, though the pattern at different stations differs in detail. Fans C and D are located closer to station 264128 than fans A and B (Figure 1), which explains the higher seismic energy for fans C and D than for fans A and B. As fans A and B located closer to the station 264114 than fans C and D, we observed higher seismic energy from fans A and B compared to that from fans C and D. The seismic response of pumps SA, SB, and SC are observed at 5–50 Hz at station 264114 and at 5–150 Hz at station 264128 (Figure 9 and Figure 10). When we filtered the seismogram with a bandpass filter of 5–50 Hz, the seismic signals show a clear correlation with pump operating status.

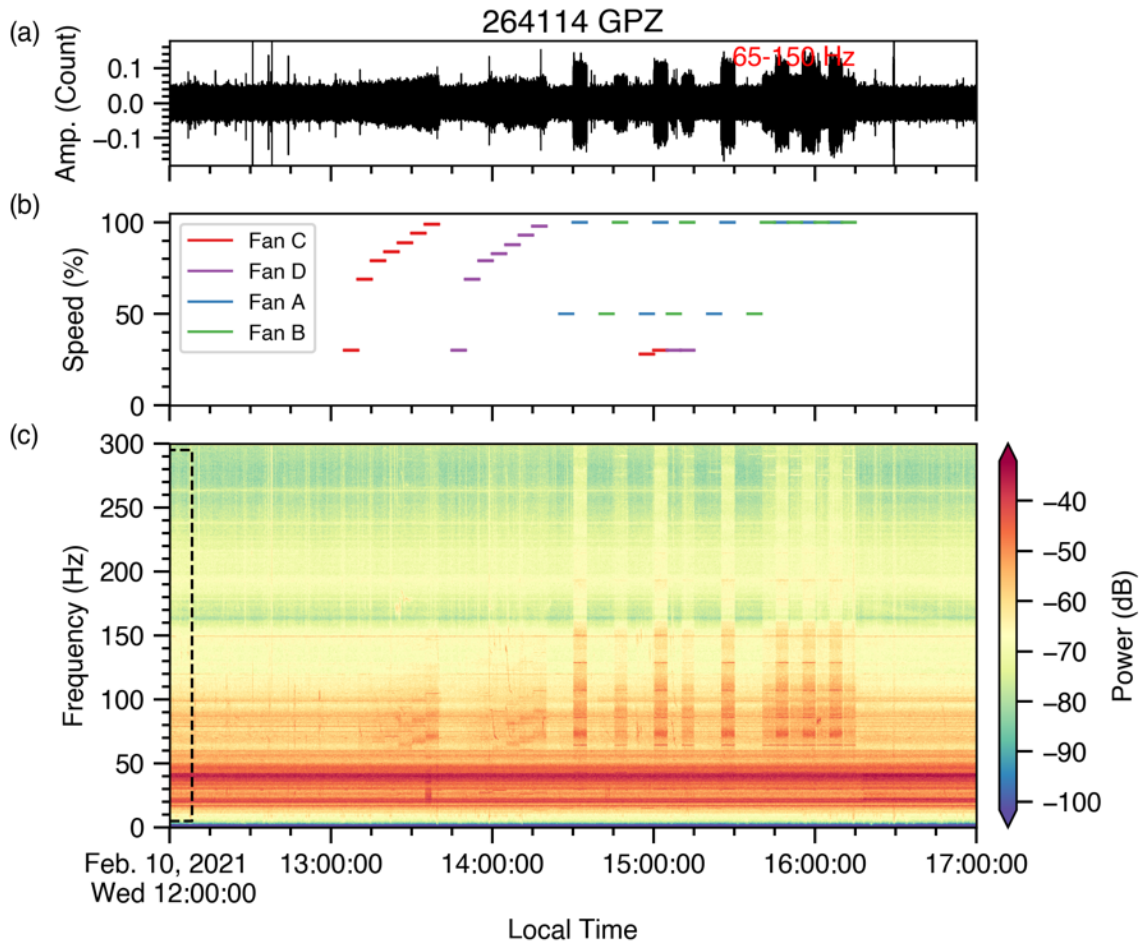

Figure 7. Seismic data recorded at the station 264114 during the fan test on February 10, 2021. The figure layout and symbols are the same as Figure 3. Note the seismic data in panel (a) were filtered with a bandpass filter between 65–150 Hz.

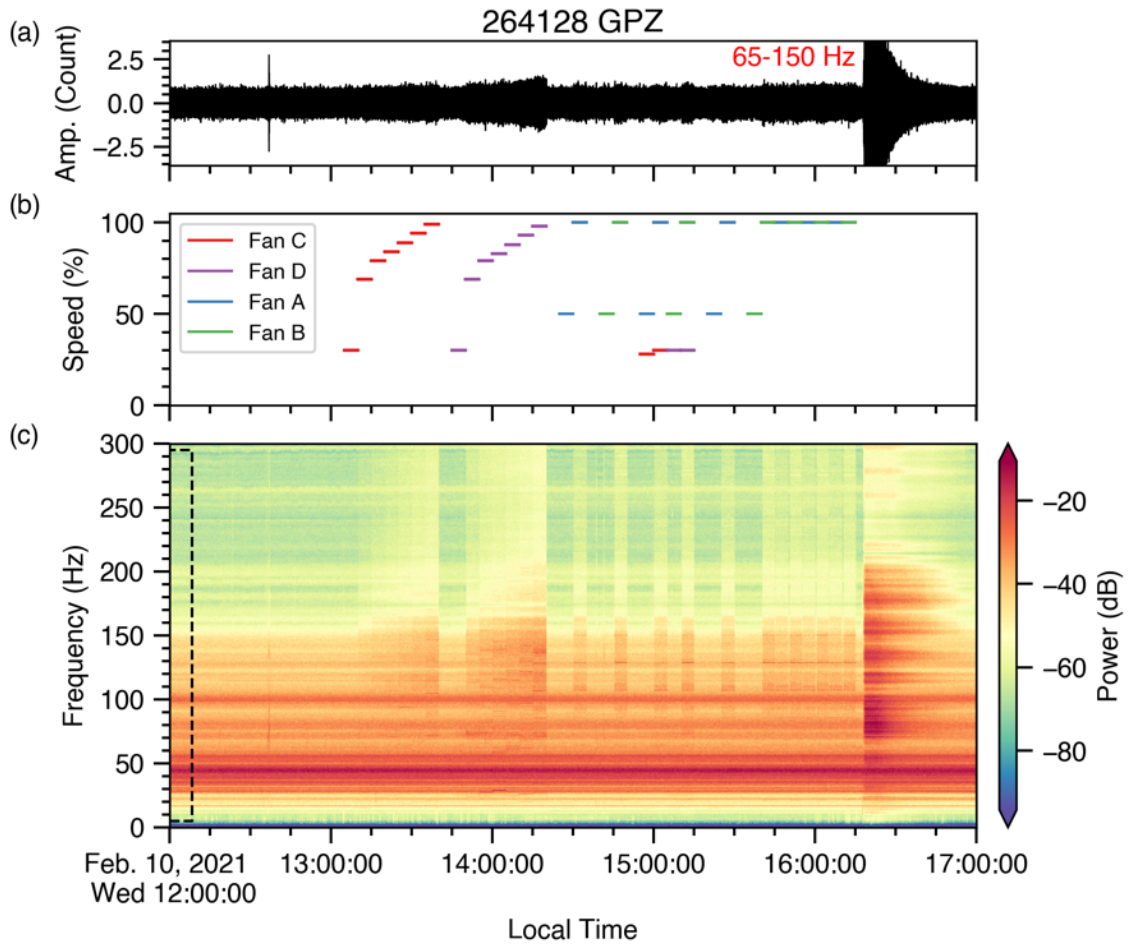

Figure 8. Seismic data recorded at the station 264128 during the fan test on February 10, 2021. The figure layout and symbols are the same as Figure 7.

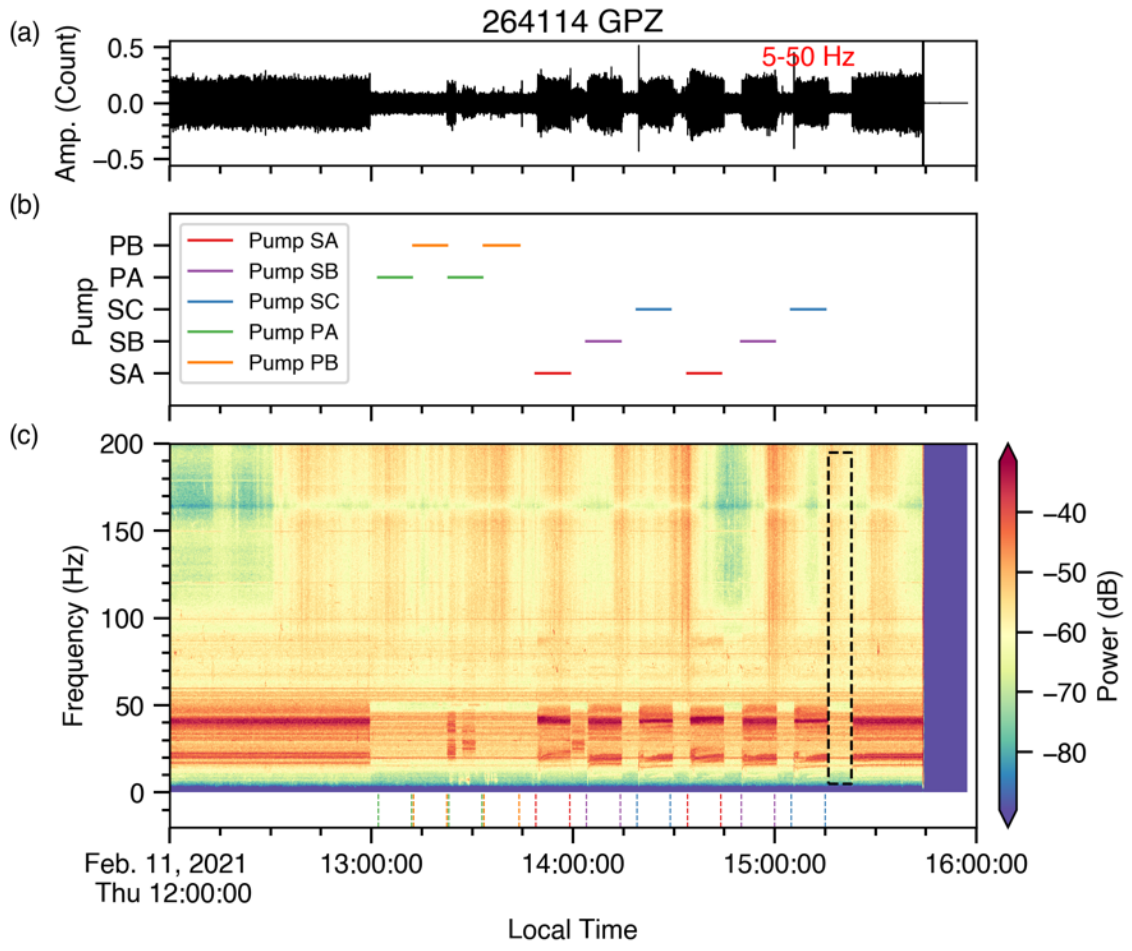

Figure 9. Seismic data recorded at the station 264114 during the pump test on February 11, 2021. Panel (a) shows the vertical-component seismogram filtered with a bandpass filter between 5 and 50 Hz. Panel (b) indicates the time when a specific pump was operating. Pumps PA and PB located inside of the main building of HFIR. Pumps SA, SB and SC are located near the cooling tower of HFIR. Panel (c) shows the spectrogram of the seismic data. The dashed vertical lines indicate when the operational state of a pump was changed. The bashed box shows the time window that was used as background.

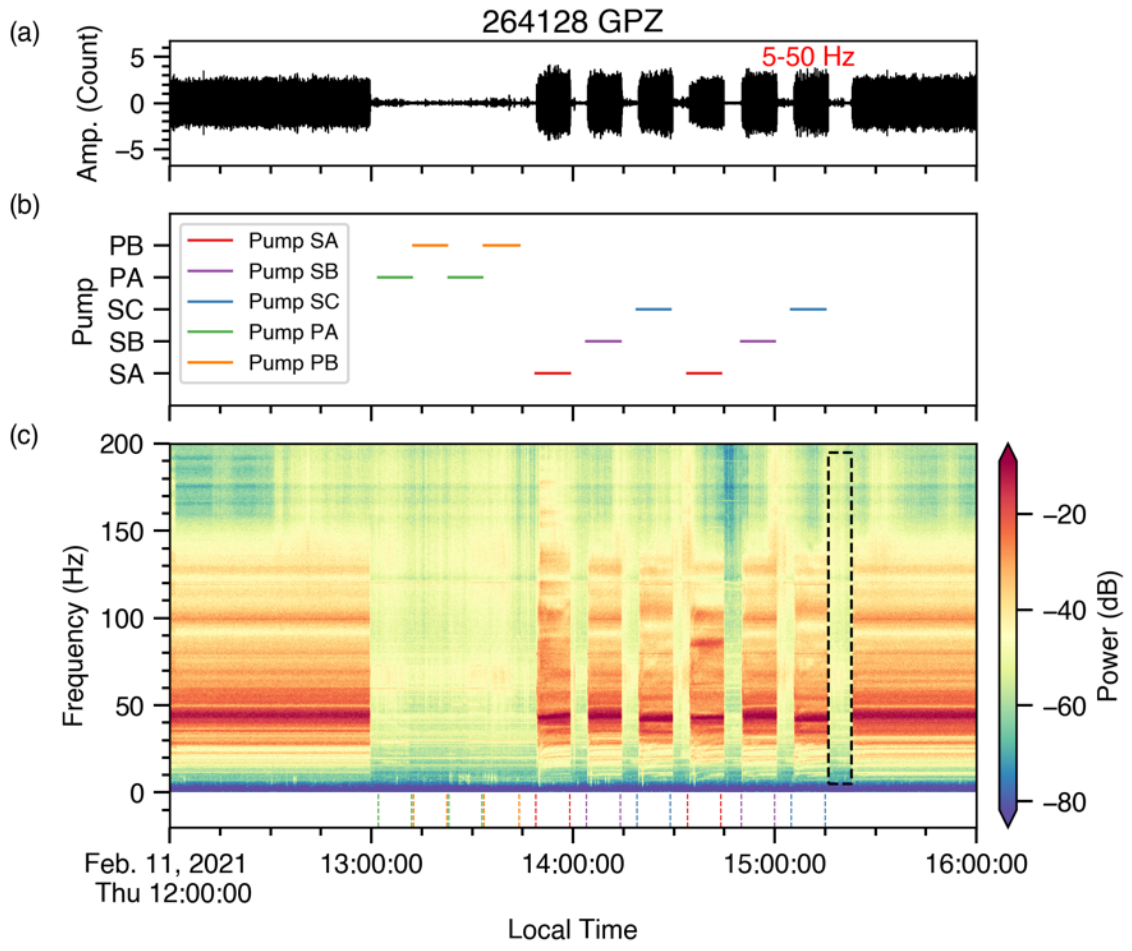

Figure 10. Seismic data recorded at the station 264128 during the pump test on February 11, 2021. The figure layout and symbols are the same as Figure 9.

4.2 POWER SPECTRAL DENSITY

PSD curves of fan C from the December 6, 2019, fan test for seismic and acoustic data are shown in Figure 11 and Figure 12, respectively. We used data in a time window prior to the fan test (dashed boxes in Figure 3 and Figure 4) as the background. By subtracting the background, the seismic and acoustic responses of different fan speed are clearly visualized (Figure 11b and Figure 12b). The interactive tool was then used to select impulsive frequencies with higher or lower amplitude. As shown in Figure 11b, different impulsive frequencies were recorded with seismic sensors for different fan speeds. Different seismic channels recorded different impulsive frequencies even when the fan speed is the same. Higher fan speed usually leads to more frequencies with large amplitudes. A similar phenomenon was observed for the other fans (Figure A1, Figure A2, and Figure A3). In addition to impulsive frequencies, we also observed broadband features (130–190 Hz) on the vertical seismograms when the fan speed was higher than 70%. This patten was observed for signals associated with other fans. Though the shape and size of these features differ significantly for different fans. We do not see such consistent patterns on horizontal seismograms. These broadband features can exist on the horizontal components at 80% fan speed in some cases. But the broadband features can be missing at 90% or 100% fan speed. As expected, more impulsive

frequencies were detected from the acoustic data (Figure 12b). Different fan speeds lead to different impulsive frequencies in acoustic data. More impulsive frequencies with large amplitudes were observed for higher fan speeds. The same trend was observed for signals associated with other fans (Figure A4, Figure A5, and Figure A6).

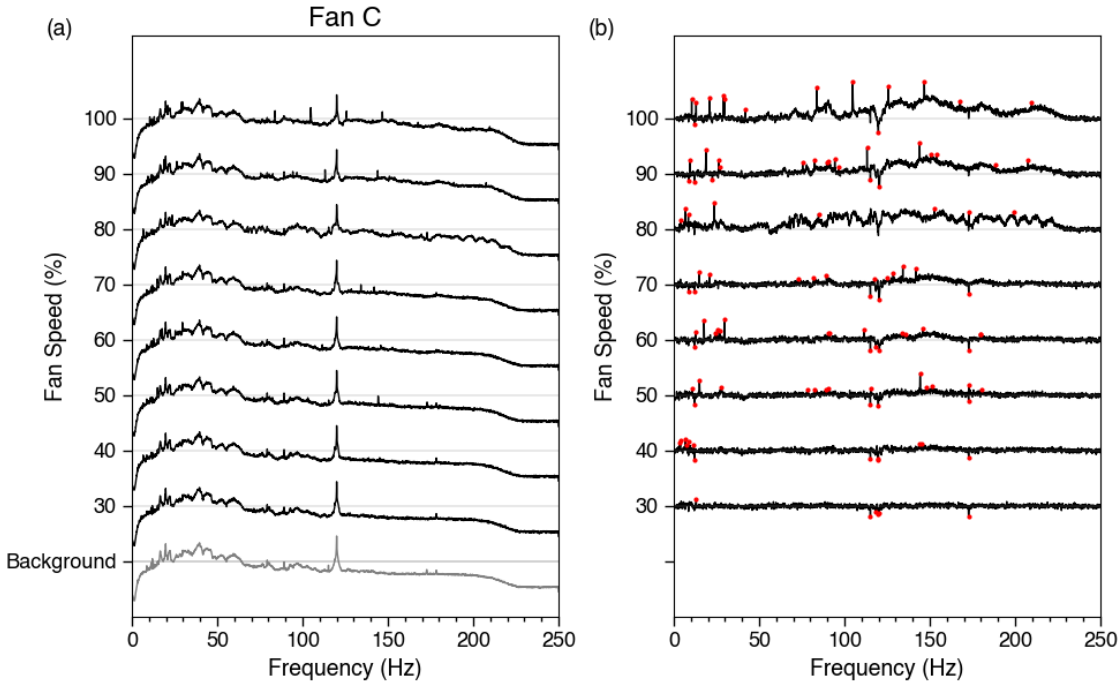

Figure 11. A comparison of PSDs for different operating speeds of Fan C using the vertical seismic data from the December 6, 2019, fan test (a) before and (b) after background removal. The red dots in panel (b) indicate data points manually selected with the interactive tool.

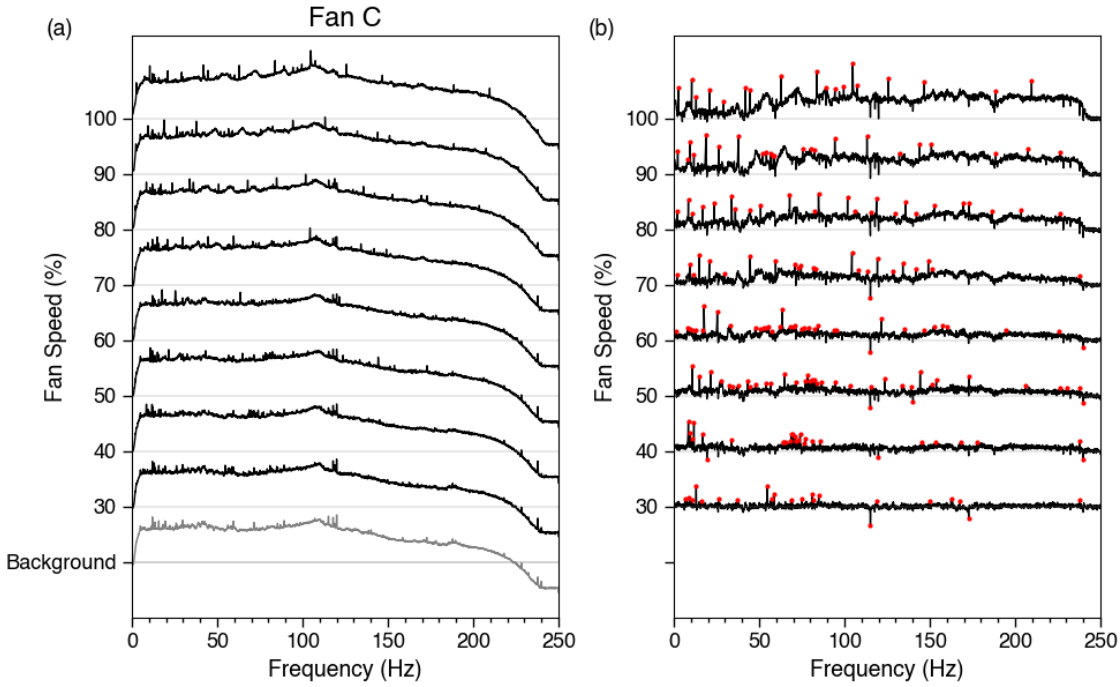

Figure 12. A comparison of PSDs for different operating speeds of Fan C using the acoustic data from the December 6, 2019, fan test (a) before and (b) after background removal. The symbols are the same as Figure 11.

Figure 13 and Figure 14 present PSD curves from the June 5, 2020, fan test for seismic data and acoustic data, respectively. Visually, we found that the PSD curves associated with two operating fans have the same characteristics as the PSD curve for one of the two operating fans but include additional features that likely originate from the other fan. We suspect the PSD curve for two operating fans were the result of a superimposition of the PSD curves for the two individual fans. To validate this, we subtracted the PSD curve corresponding to one of the two operating fans from the PSD curve corresponding to the two fans. The resulting PSD curve is referred to as the *derived PSD*. Comparing the directly observed PSD curve and derived PSD curves for fan C at 80% speed, we found they are consistent for both seismic and acoustic data (Figure 15 and Figure 16) to a first approximation. Specifically, the seismic PSDs show impulsive responses associated with fan C at 80% speed at 23.6, 101.8, and 152.7 Hz for both directly observed PSD curve and derived PSD curves. The acoustic PSDs contain impulsive responses associated with fan C at 80% speed at 8.6, 17.0, 33.9, 36.1, 67.9, 84.8, 101.8, 118.8, 135.7, 152.7, and 203.6 Hz.

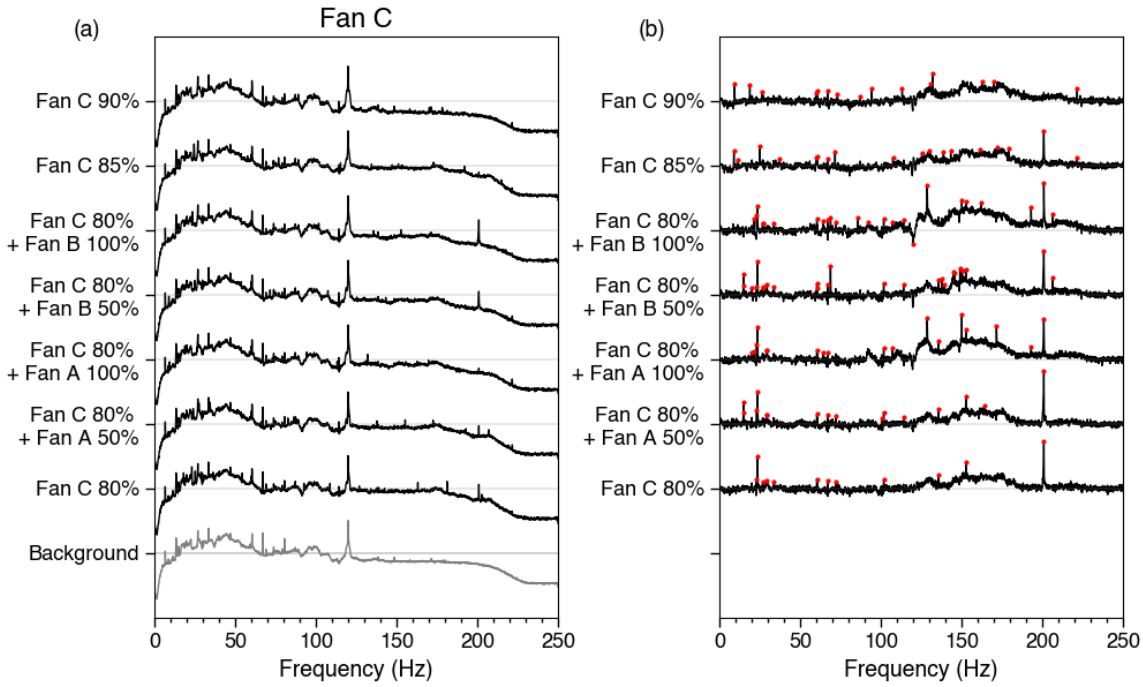

Figure 13. A comparison of PSDs for different operating speeds of Fan C using the seismic data from the June 5, 2020, fan test (a) before and (b) after background removal. The symbols are the same as Figure 11.

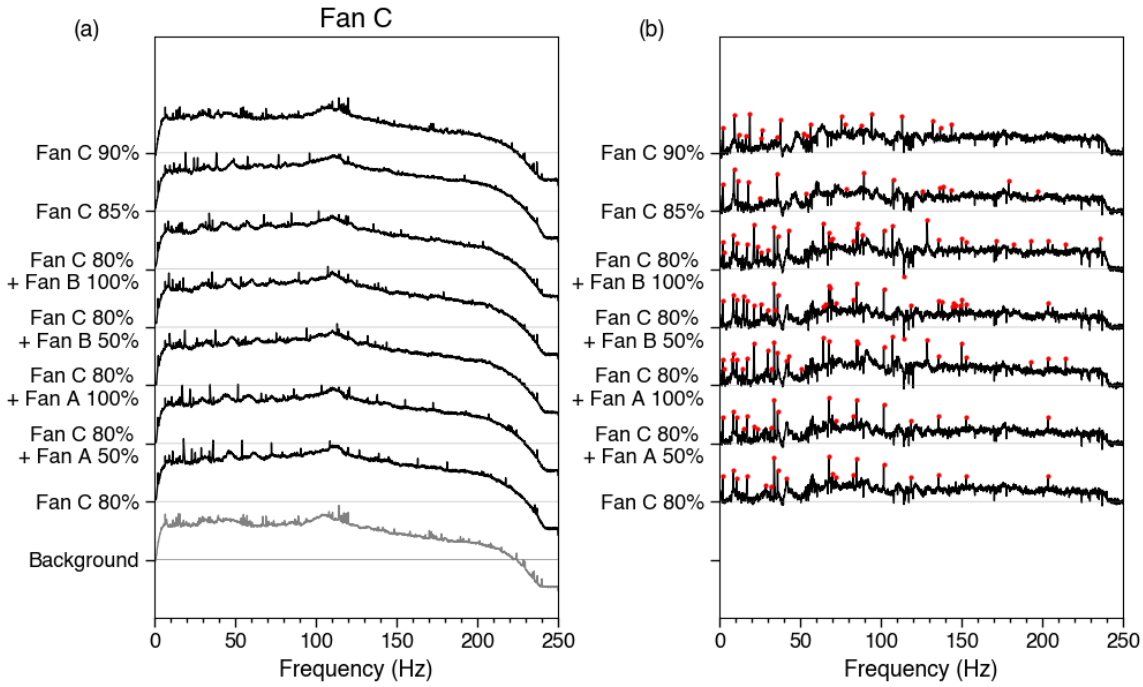

Figure 14. A comparison of PSDs for different operating speeds of Fan C using the acoustic data from the June 5, 2020, fan test (a) before and (b) after background removal. The symbols are the same as Figure 11.

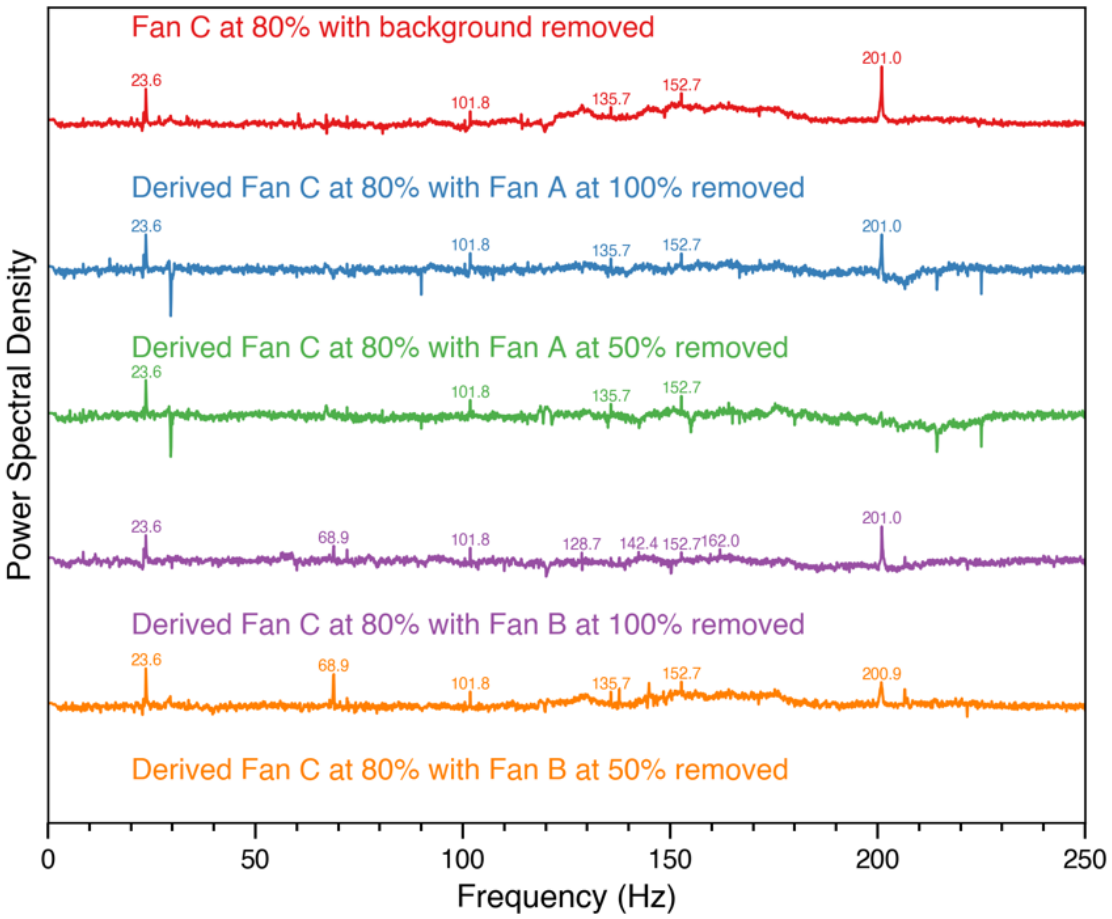

Figure 15. A comparison of directly observed and derived PSDs of the vertical seismic chancel for signals associated with the fan C at 80% speed from the fan test on June 5, 2020. The derived PSDs were obtained by subtracting the PSD for one operating fan from the PSD for two fans operating simultaneously.

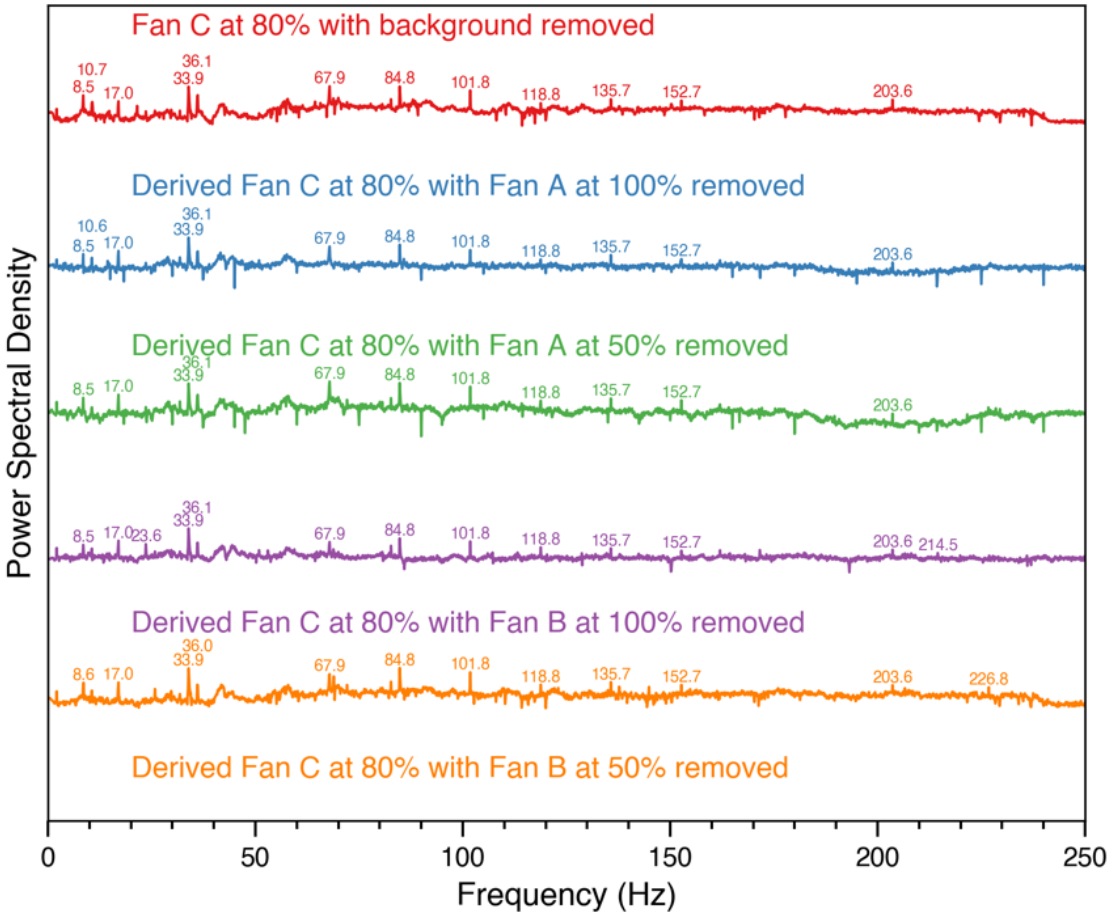

Figure 16. A comparison of directly observed and derived PSDs of the acoustic chancel for signals associated with the fan C at 80% speed from the fan test on June 5, 2020. The derived PSDs were obtained by subtracting the PSD for one operating fan from the PSD for two fans operating simultaneously.

We compared the acoustic PSDs from the fan test on December 6, 2019, against the staring of the HFIR operating cycles 485A (started on December 17, 2019), 485B (started on January 3, 2020), and 486 (started on January 30, 2020). The root mean square (RMS) difference between the PSD curves associated with each fan and at each tested speed and the PSD curves corresponding to the beginning of each operating cycle. As shown in Figure 17, the RMS difference for cycles 485A and 485B are minimum when compared against fan D at 100% speed. On the other hand, the RMS difference for cycle 486 is the smallest when compared to fan C at 100% speed. These results suggest fan C may have played a major role at the beginning of cycles 485A and 485B. Of the four fans, fan D may have contributed the most at the beginning of cycle 486. More detailed signal comparisons are shown in Figure 18, Figure 19, and Figure 20 for cycles 485A, 485B, and 486, respectively. The match between the signal from the fan test on December 6, 2019, and the signal from the operating cycles is reasonable.

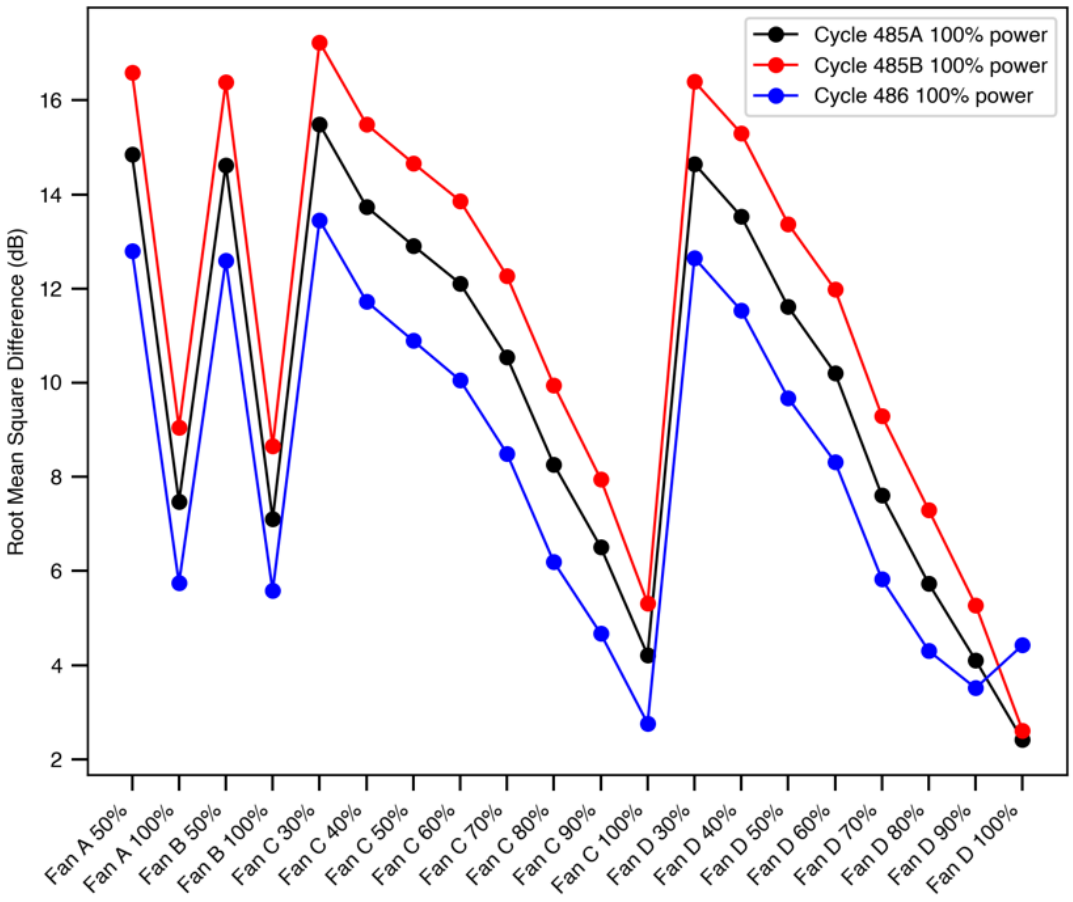

Figure 17. The root-mean-square difference between the acoustic PSD from the fan test on December 6, 2019, and that from the starting of the HFIR operating cycles 485A, 485B, and 486.

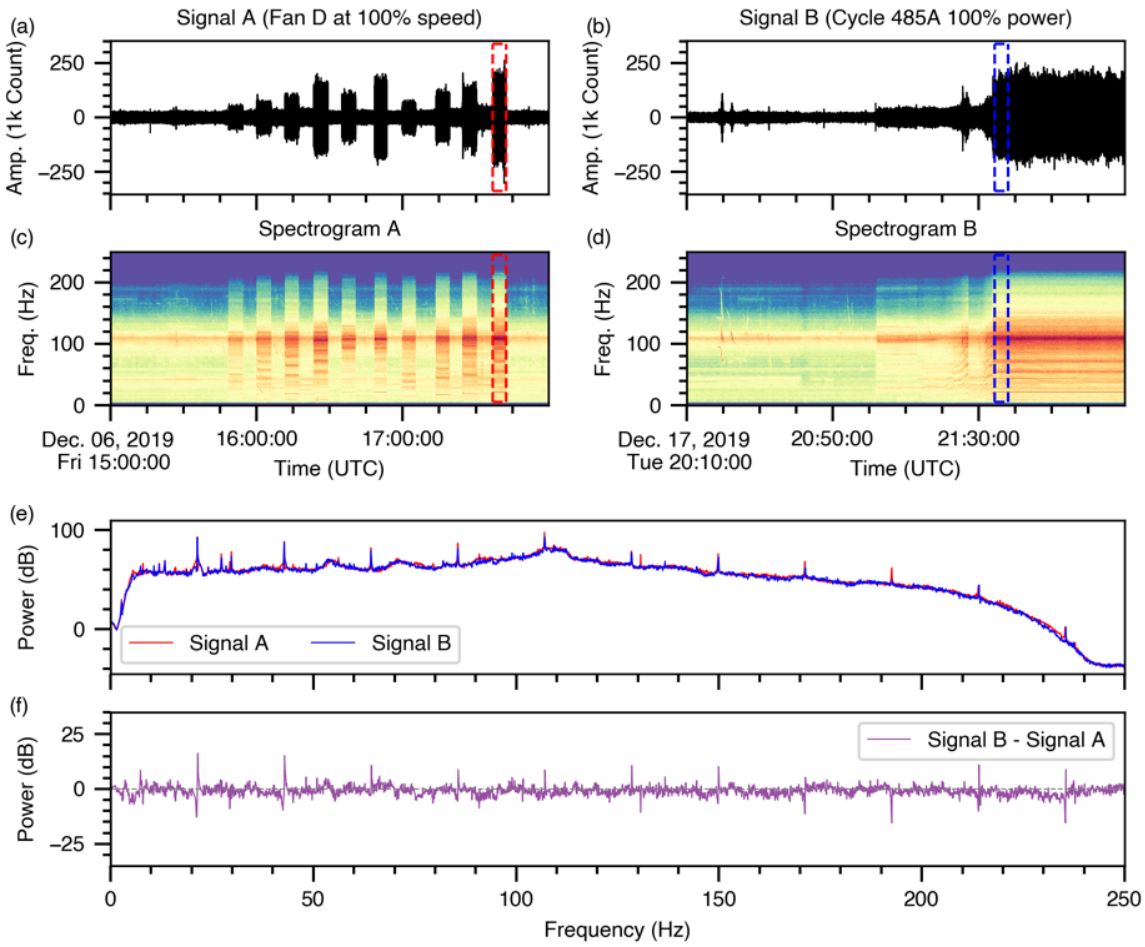

Figure 18. A comparison of the acoustic signal associated with fan D at 100% speed against the signal corresponding to 100% power level of HFIR operating cycle 485A. Panels (a) and (b) show the signals in time domain. Panels (c) and (d) show the spectrogram of the corresponding signals of the dashed boxes in (a) and (b), respectively. Panels (e) and (f) present PSDs of both signals and their difference.

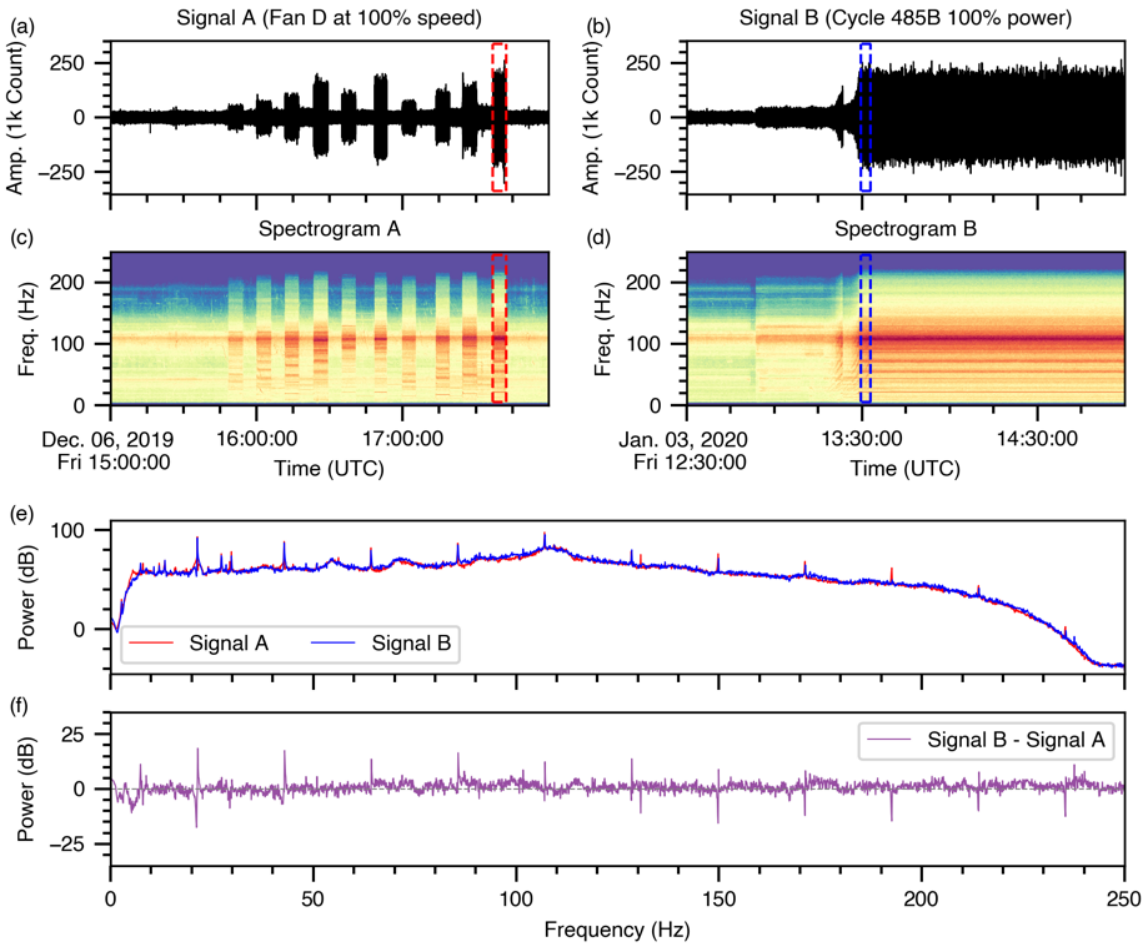

Figure 19. A comparison of the acoustic signal associated with fan D at 100% speed against the signal corresponding to 100% power level of HFIR operating cycle 485B. The figure layout is the same as Figure 18.

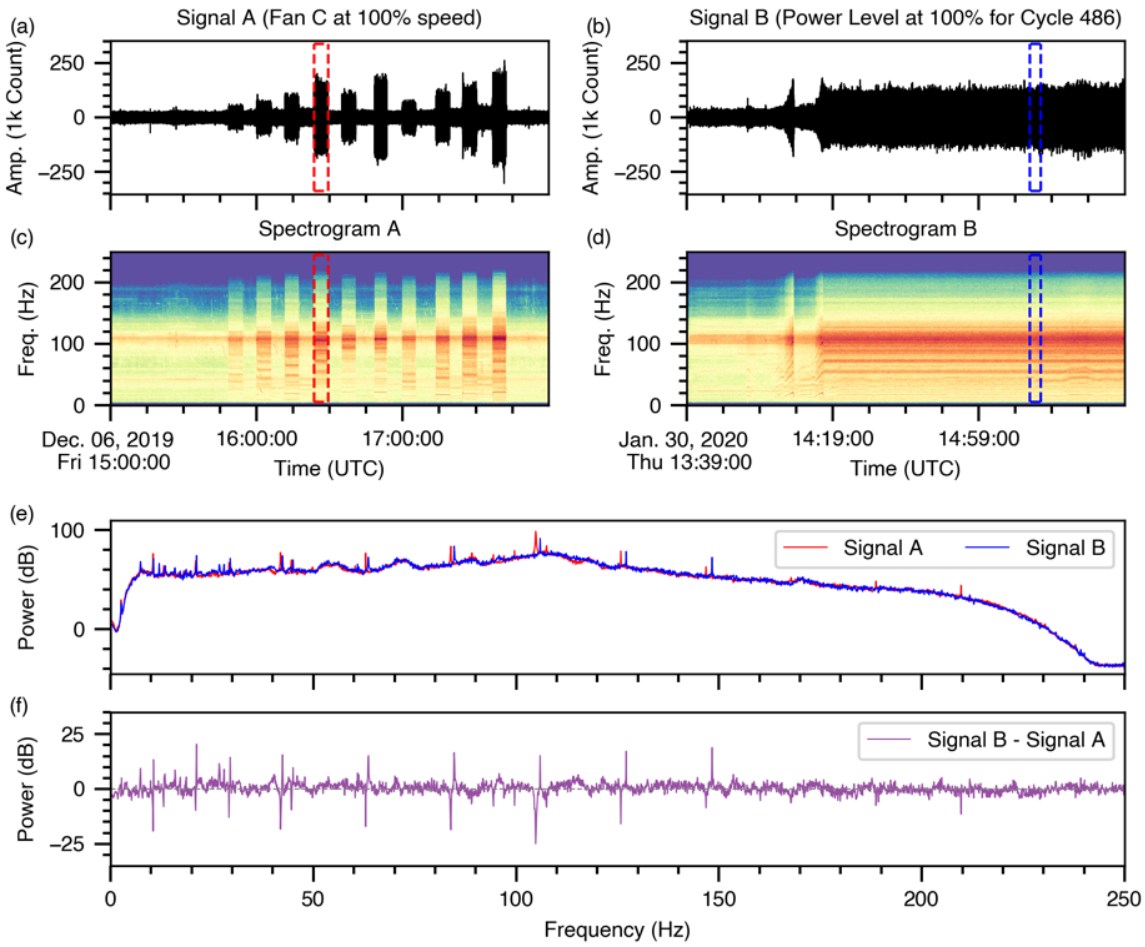

Figure 20. A comparison of the acoustic signal associated with fan C at 100% speed against the signal corresponding to 100% power level of HFIR operating cycle 486. The figure layout is the same as Figure 18.

The seismic PSDs from the February 10, 2021, fan tests at two stations (264114 and 264128) are shown in Figure 21. The selected PSD frequencies using the interactive tool show noticeable differences between the two stations. However, common PSD frequencies exist between the two stations for most cases (Figure 22). Unlike the fans, operations of pumps SA, SB, and SC led to broadband changes in PSD (Figure 23). At station 264114, the changes in PSD due to pump operations mostly occurred in the frequency band of 5–50 Hz. At station 264128, the PSDs show largest differences in the frequency band of 5–150 Hz. The seismic responses of pumps SA, SB, and SC are similar to the first order.

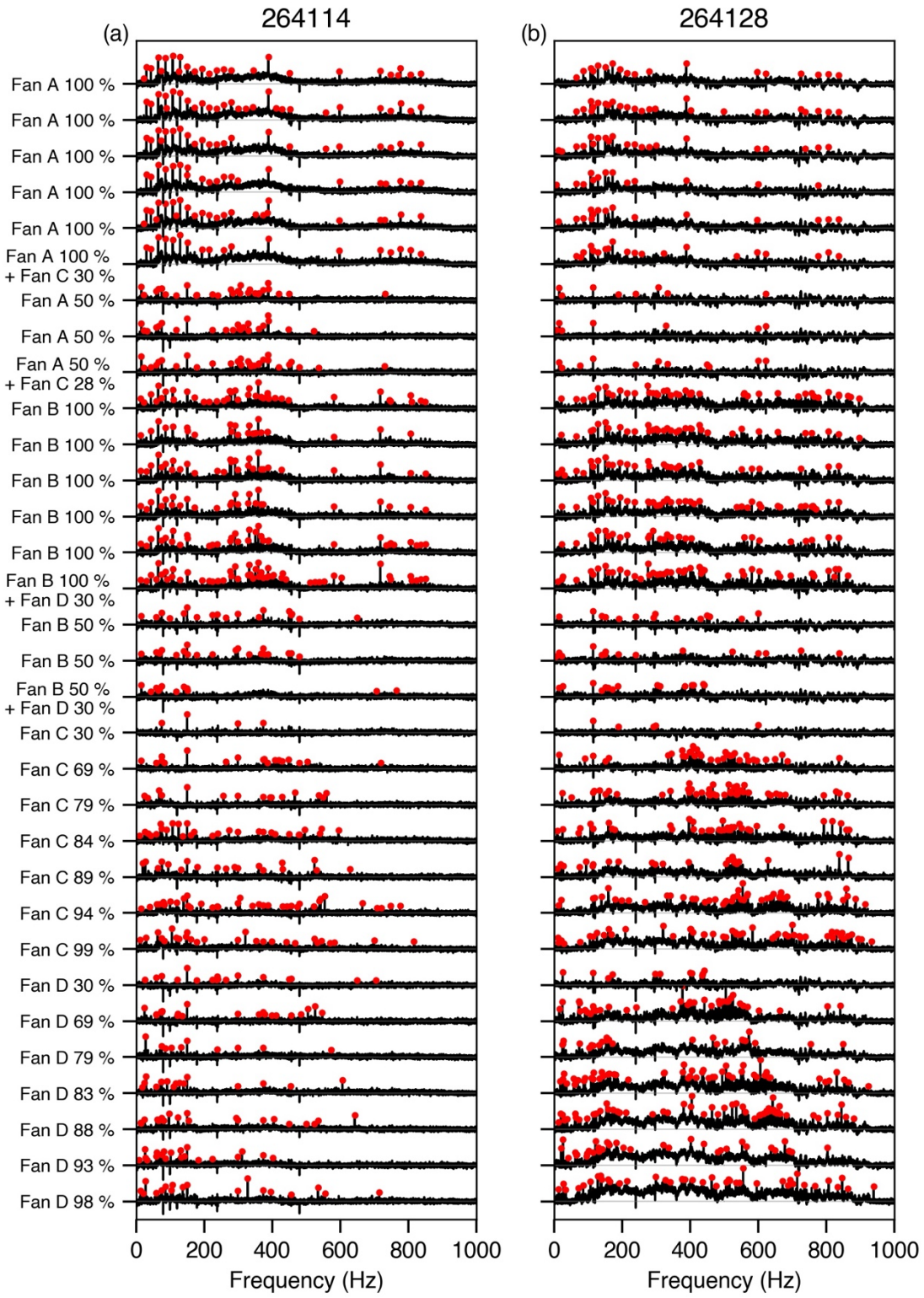

Figure 21. A comparison of PSDs for different fans at different operating speed using the vertical seismic data from the February 10, 2021, fan test for (a) the station 264114 and (b) the station 264128. The red dots indicate data points manually selected with the interactive tool. Black lines show PSDs after background removal.

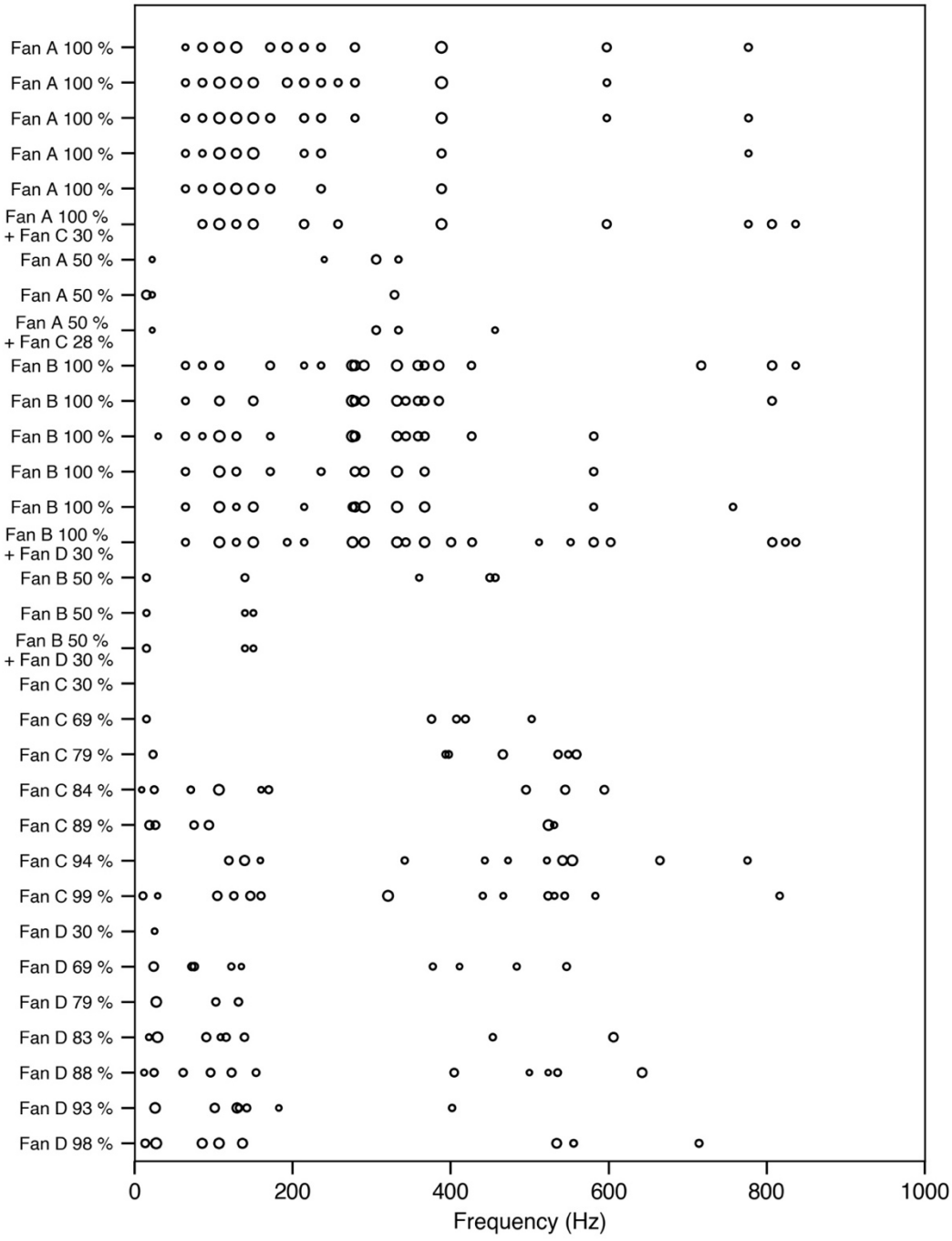

Figure 22. Common PSD frequencies (circles) that were selected for both stations (264114 and 264128) for different fans at different operating speed. The size of the circles is proportional to the minimum PSD amplitude from the two stations. When a red dot in Figure 21a and a red dot in Figure 21b have the same frequency, a circle at the frequency is plotted in this figure.

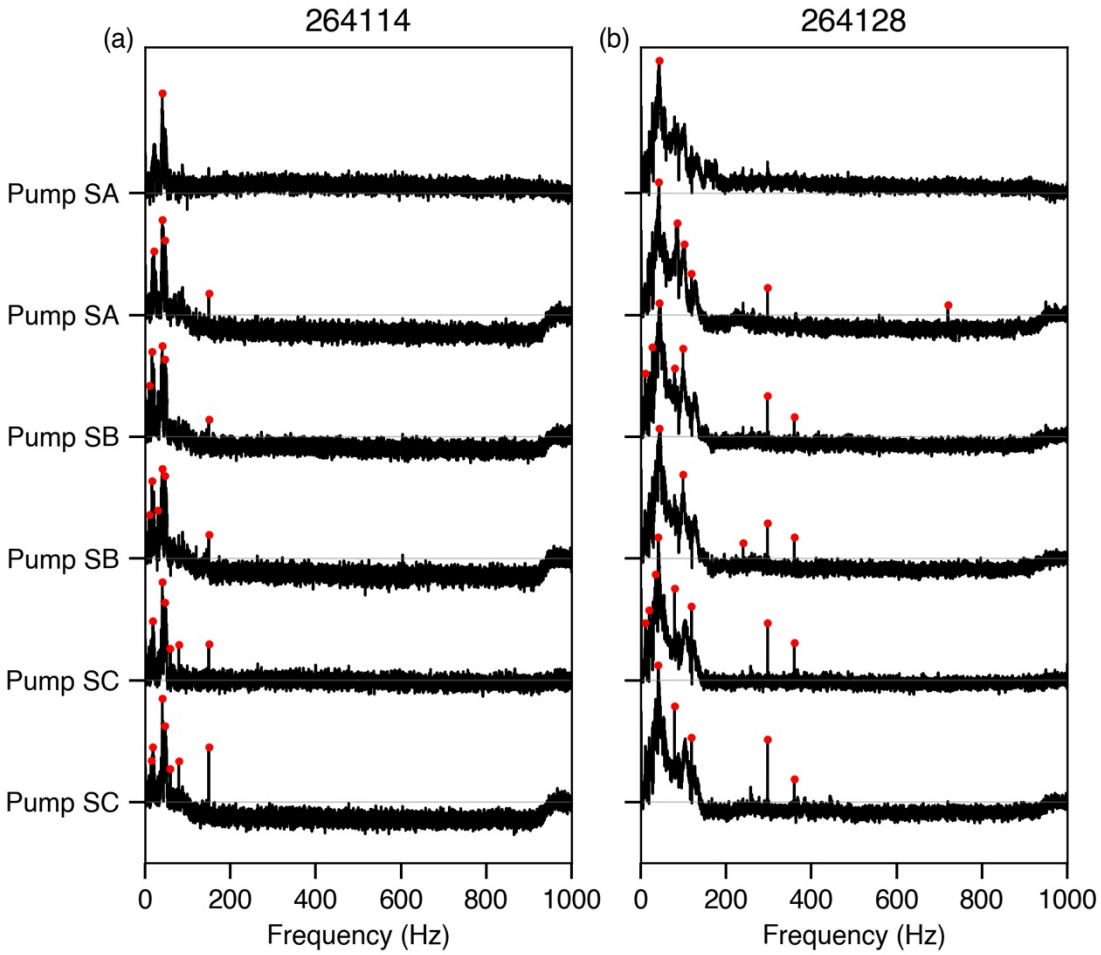

Figure 23. A comparison of PSDs for different pumps using the vertical seismic data from the February 11, 2021, pump test for (a) the station 264114 and (b) the station 264128. The red dots indicate data points manually selected with the interactive tool. Black lines show PSDs after background removal.

4.3 SOURCE LOCATION

The observed absolute signal amplitudes of the vertical seismic data associated with a cooling tower pump exhibited an expected decay as a function of source-to-receiver distance (Figure 24). The recorded seismic amplitude is the largest at station 264112. The predicted seismic amplitudes using the actual location (measured from the Google Earth satellite image in Figure 1) matched the observations well. The RMS errors from the grid search identified regions where the source is likely located. The region outlined by the dashed line in Figure 25a has RMS errors similar to that of Figure 24. The source is expected to locate in this half-ring-shaped region centered at station 264112 with a radius of about 15 m. The seismic data–inferred source location contains the actual location of the pump.

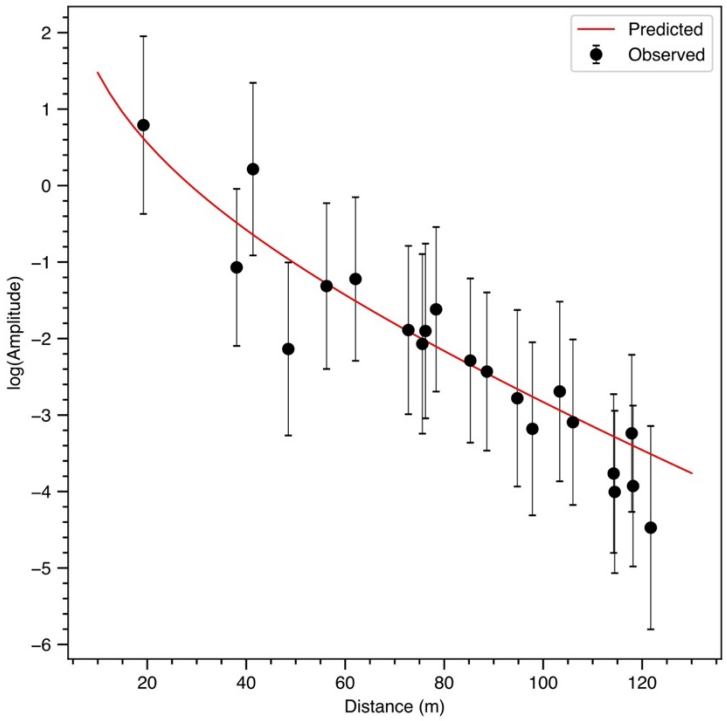

Figure 24. The observed and predicted seismic amplitude as a function of source-to-receiver distance using data from the pump test on February 11, 2021. The pump location in Figure 25b was used to compute the source-to-receiver distances and predict the seismic amplitudes.

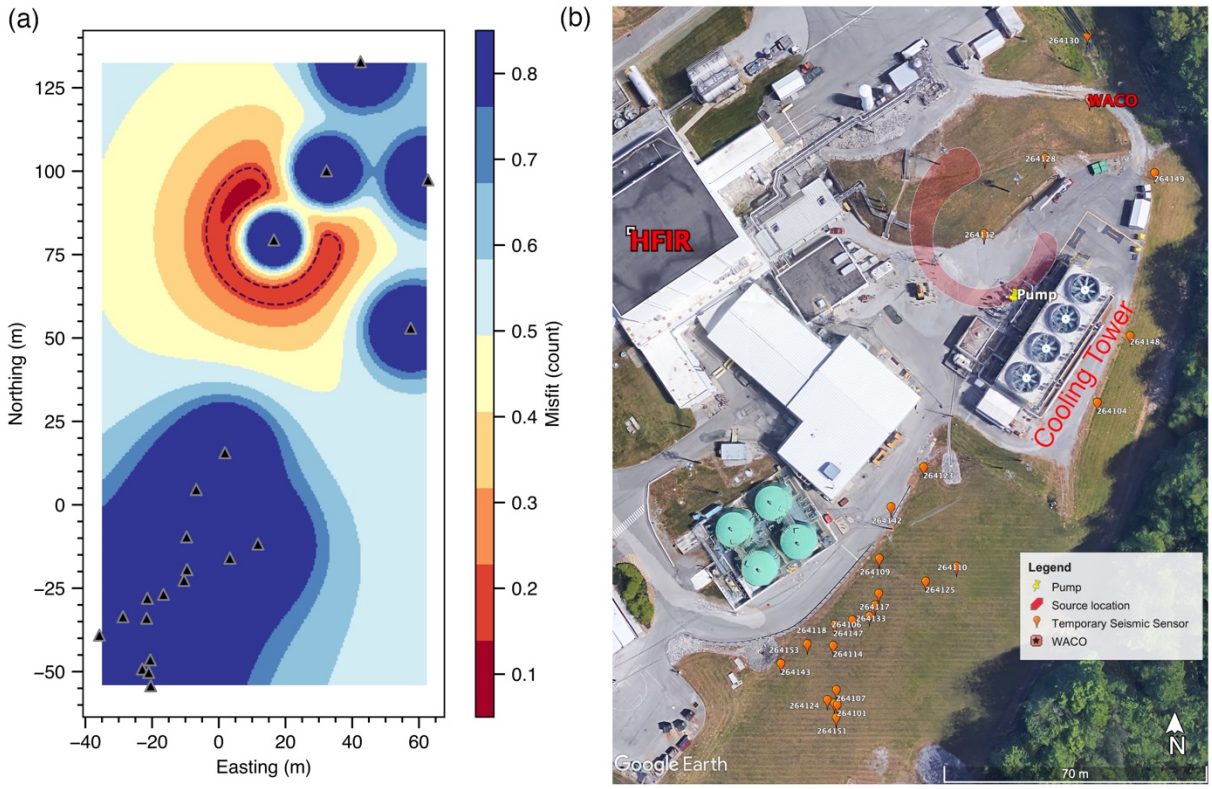

Figure 25. The location of the mechanical source estimated using seismic signals associated with a cooling tower pump shown in (a) a local coordinate system (dashed line) and (b) a Google Earth satellite image (red shaded region). The dashed line in panel (a) represents a contour with a misfit of 0.2. The triangles in panel (a) indicate temporary seismic sensors. The red shaded region in panel (b) corresponds to the region outlined by the dashed line in panel (a).

5. CONCLUSION AND DISCUSSION

The seismo-acoustic data from the December 6, 2019, and June 5, 2020, fan tests show clear seismic and acoustic responses of both the fixed-speed fans (A and B) and variable-speed fans (C and D) at the WACO station. The responses are more visible in frequency domain (spectrogram). The fan-related signals are clearer in acoustic channels than in the seismic channels with a simpler background. The seismic channels contain signals from unknown sources and a more complicated background. As expected, the fan-related responses are stronger in both seismic and acoustic channels for faster fan speeds. At different fan speeds, different impulsive responses were observed in the frequency domain. These impulsive frequencies that correspond to fans are more easily identified when the background is removed, and the interactive tool has been quite helpful for picking the impulsive frequencies.

Seismic responses from the four cooling tower fans and three pumps were observed at all the seismic stations deployed on February 10, 2021, and February 11, 2021. We did not see seismic signals corresponding to two pumps that are located inside of HFIR main building. Faster fan speeds correlate with higher seismic energy. As expected, the seismic energy is higher when the source-to-sensor distance is smaller. A stepwise increase in fan speed led to a stepwise pattern in the seismic spectrogram. Seismic responses from the same fan at the same operating speed show differences at different stations, while common impulsive frequencies exist in most cases. The seismic responses due to pump operations led to

broadband changes in PSD rather than impulsive frequencies. The responses from the three pumps show similar characteristics in the frequency domain.

Using data from the pump test on February 11, 2021, we estimated the source location of one pump related event using absolute seismic amplitudes. The largest seismic amplitude was recorded at the station 264112, which suggests that the source is located near that station. By performing a grid search of source locations, we were able to identify a half-ring-shaped region centered at station 264112 where the source is likely located, which included the actual location of the pump. The width of the ring is about 5 m. The ring shape is likely due to the limited azimuthal coverage, especially in the northwest direction. A directional analysis of the source at the station 264112 that uses a three-component seismic signal may reduce the source location uncertainty by providing additional azimuthal constraints.

6. ACKNOWLEDGEMENTS

The work described in this paper was funded by the US National Nuclear Security Administration, Office of Defense Nuclear Nonproliferation Research and Development, Office of Proliferation Detection. This manuscript has been authored in part by UT-Battelle, LLC, under contract DE-AC05-00OR22725 with the US Department of Energy (DOE). This research used resources at the High Flux Isotope Reactor, a DOE Office of Science User Facility operated by the Oak Ridge National Laboratory.

This research used resources of the Compute and Data Environment for Science (CADES) at the Oak Ridge National Laboratory, which is supported by the Office of Science of the US Department of Energy under Contract No. DE-AC05-00OR22725.

The views and conclusions contained in this document are those of the authors and should not be interpreted as necessarily representing the official policies, either expressed or implied, of the U.S. Government. The authors acknowledge that there are no conflicts of interest recorded.

Most figures were prepared with Matplotlib version 3.4.3 (Hunter 2007). Numpy version 1.21.2 (Van Der Walt, Colbert, and Varoquaux 2011) and ObsPy version 1.2.2 (Megies et al. 2011; Krischer et al. 2015; Beyreuther et al. 2010) were used to process the seismic and acoustic data. Figure 1 and Figure 25 used satellite images from Google Earth (https://www.google.com/earth/, last accessed on September 2021). The PSD frequency picker was developed with Bokeh 2.2.3 (https://www.bokeh.org, last accessed on September 2021).

7. REFERENCES

Beyreuther, M., R. Barsch, L. Krischer, T. Megies, Y. Behr, and J. Wassermann. 2010. “ObsPy: A Python Toolbox for Seismology.” *Seismological Research Letters* 81 (3): 530–33. https://doi.org/10.1785/gssrl.81.3.530.

Chai, Chengping, Charles J. Ammon, Monica Maceira, and Robert B. Herrmann. 2018. “Interactive Visualization of Complex Seismic Data and Models Using Bokeh.” *Seismological Research Letters* 89 (2A): 668–76. https://doi.org/10.1785/0220170132.

Guenaga, David L., Chengping Chai, Monica Maceira, Omar E. Marcillo, and Aaron A. Velasco. 2021. “Seismically Detecting Nuclear Reactor Operations Using a Power Spectral Density (PSD) Misfit Detector.” *Bulletin of the Seismological Society of America* 111 (3): 1378–91. https://doi.org/10.1785/0120200267.

Hunter, John D. 2007. “Matplotlib: A 2D Graphics Environment.” *Computing in Science & Engineering* 9 (3): 90–95. https://doi.org/10.1109/MCSE.2007.55.

Krischer, Lion, Tobias Megies, Robert Barsch, Moritz Beyreuther, Thomas Lecocq, Corentin Caudron, and Joachim Wassermann. 2015. "ObsPy: A Bridge for Seismology into the Scientific Python Ecosystem." *Computational Science & Discovery* 8 (1): 014003. https://doi.org/10.1088/1749-4699/8/1/014003.

Marcillo, Omar E., and Jonathan MacCarthy. 2020. "Mapping Seismic Tonal Noise in the Contiguous United States." *Seismological Research Letters* 91 (3): 1707–16. https://doi.org/10.1785/0220190355.

Marcillo, Omar E, Monica Maceira, Chengping Chai, Christine Gammans, Riley Hunley, and Chris Young. 2021. "The Local Seismoacoustic Wavefield of a Research Nuclear Reactor and Its Response to Reactor Power Level." *Seismological Research Letters* 92 (1): 378–87. https://doi.org/10.1785/0220200139.

Megies, Tobias, Moritz Beyreuther, Robert Barsch, Lion Krischer, and Joachim Wassermann. 2011. "ObsPy—What Can It Do for Data Centers and Observatories?" *Annals of Geophysics* 54 (1): 47–58. https://doi.org/10.4401/ag-4838.

Snow, D. J. 1997. "Noise Control in Power Plant." *Proceedings of the Institution of Mechanical Engineers, Part A: Journal of Power and Energy* 211 (1): 73–93. https://doi.org/10.1243/0957650971537015.

Walt, Stéfan Van Der, S. Chris Colbert, and Gaël Varoquaux. 2011. "The NumPy Array: A Structure for Efficient Numerical Computation." *Computing in Science and Engineering* 13 (2): 22–30. https://doi.org/10.1109/MCSE.2011.37.

APPENDIX A. PSD RESULTS FOR FAN A, B, AND D

APPENDIX A. PSD RESULTS FOR FAN A, B, AND D

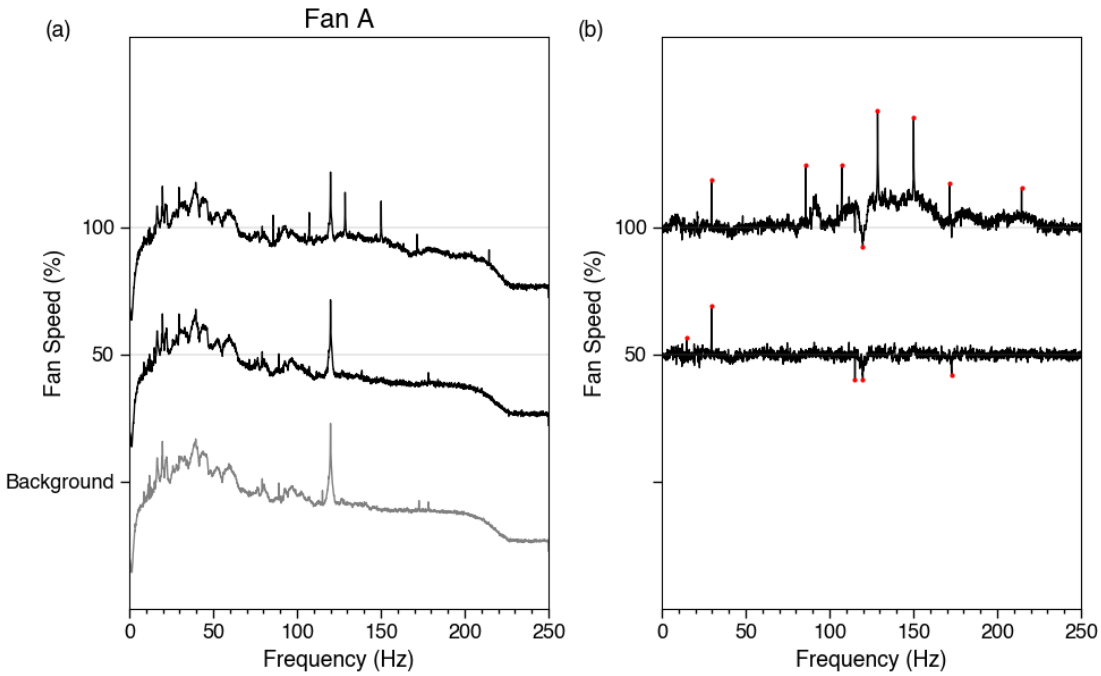

Figure A1. A comparison of different operating speed for Fan A using the vertical seismic data from the December 6, 2019 fan test (a) before and (b) after background removal. The symbols are the same as Figure 11.

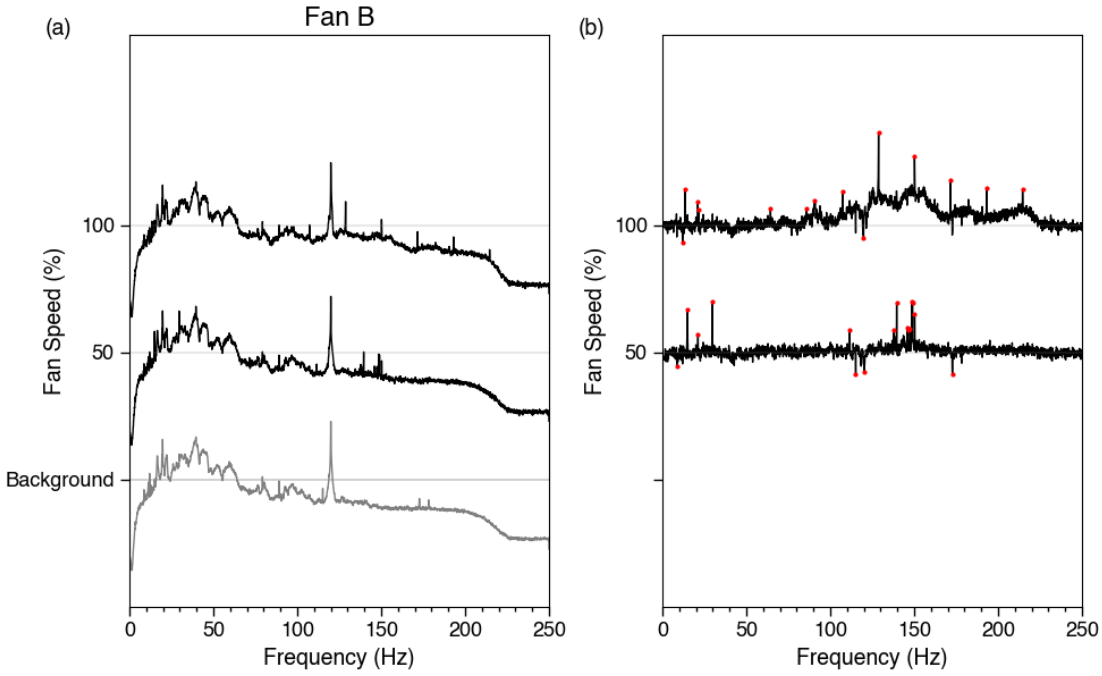

Figure A2. A comparison of different operating speed for Fan B using the vertical seismic data from the December 6, 2019, fan test (a) before and (b) after background removal. The symbols are the same as Figure 11.

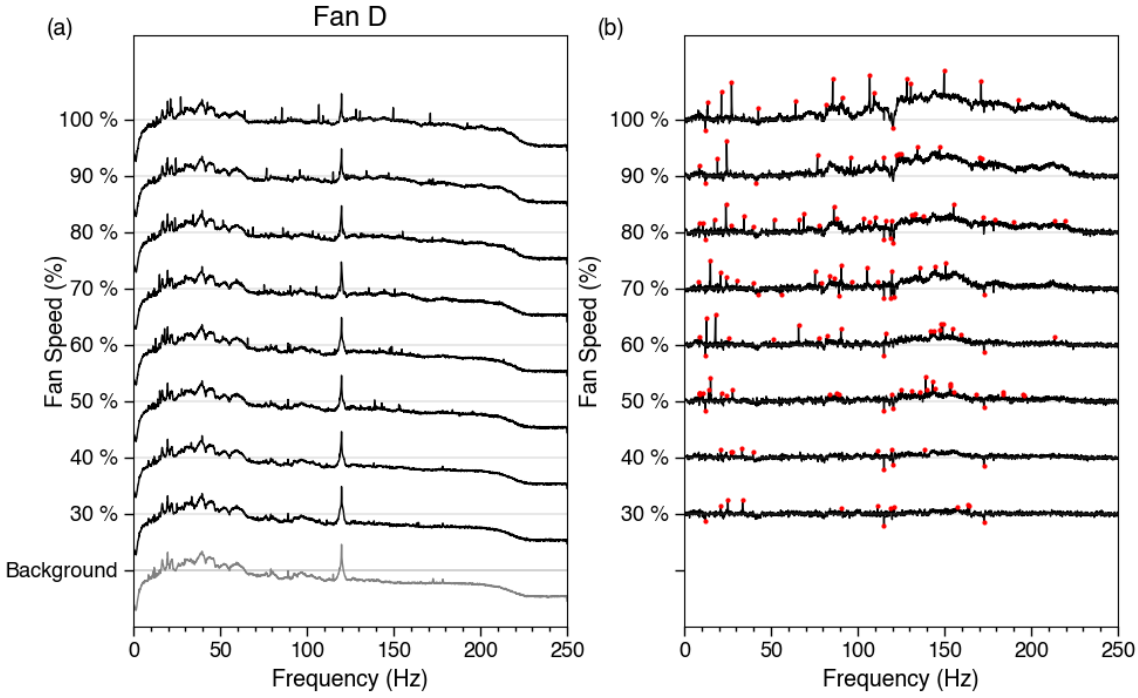

Figure A3. A comparison of different operating speed for Fan D using the vertical seismic data from the December 6, 2019, fan test (a) before and (b) after background removal. The symbols are the same as Figure 11.

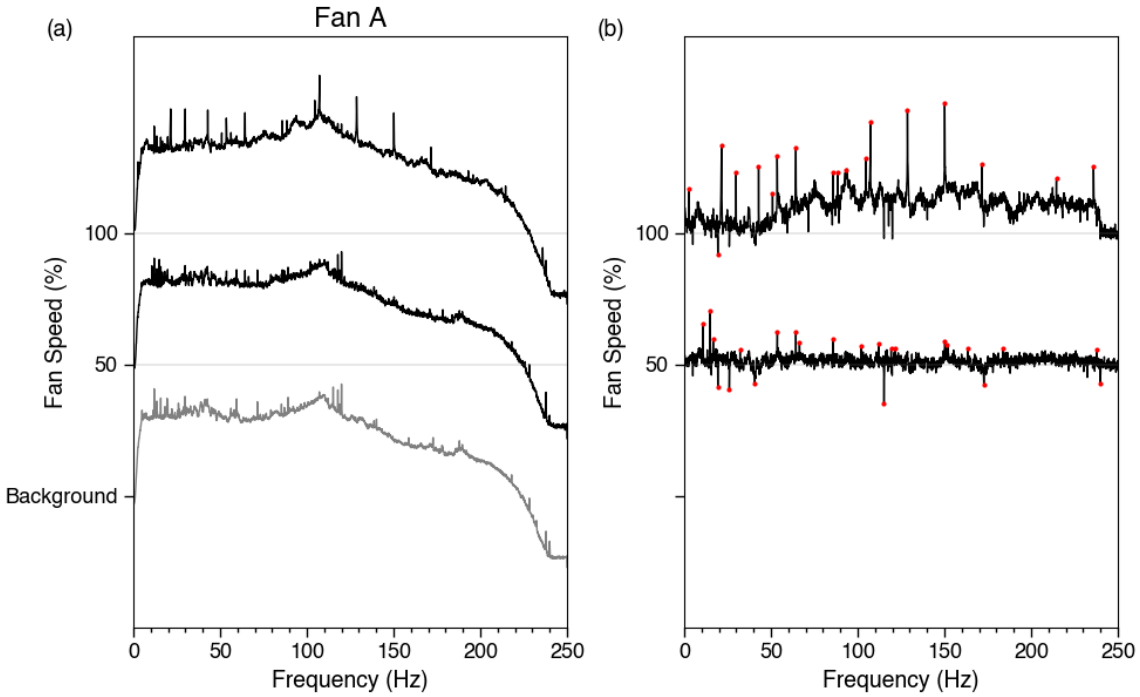

Figure A4. A comparison of different operating speed for Fan A using the acoustic data from the December 6, 2019, fan test (a) before and (b) after background removal. The symbols are the same as Figure 11.

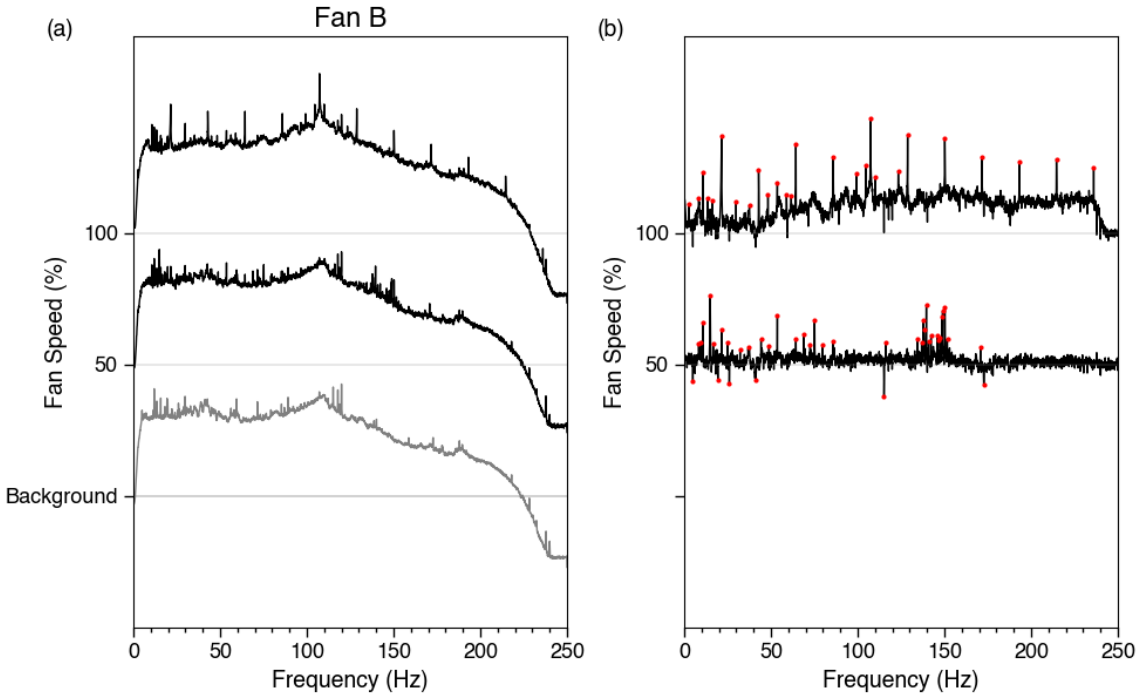

Figure A5. A comparison of different operating speed for Fan B using the acoustic data from the December 6, 2019, fan test (a) before and (b) after background removal. The symbols are the same as Figure 11.

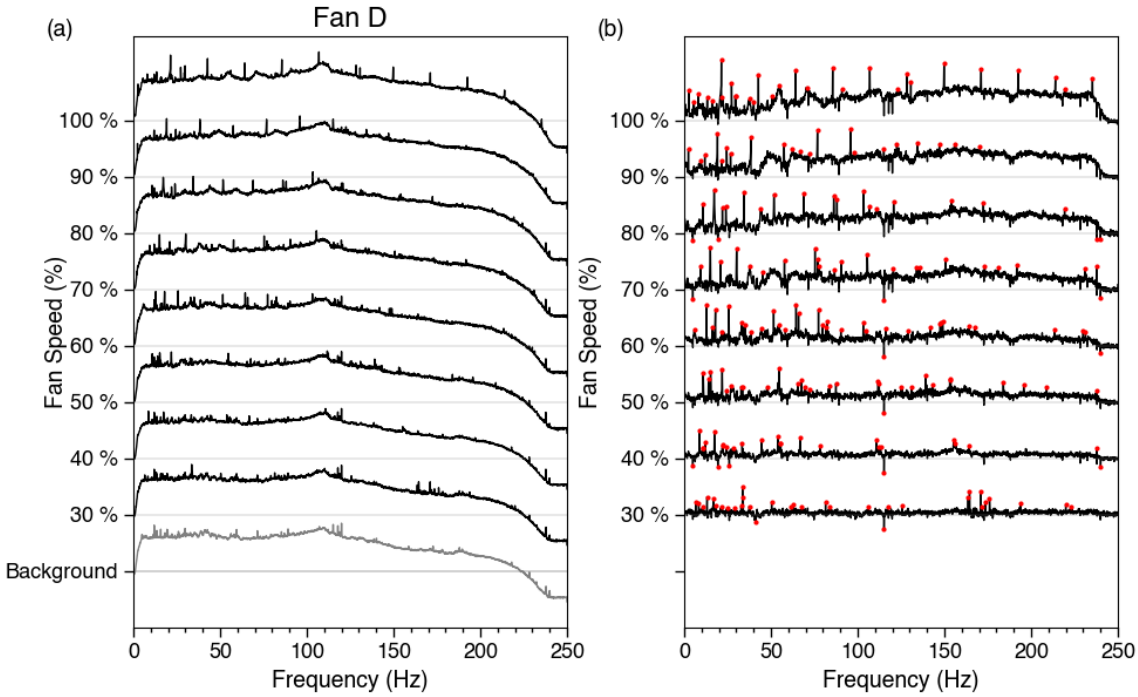

Figure A6. A comparison of different operating speed for Fan D using the acoustic data from the December 6, 2019, fan test (a) before and (b) after background removal. The symbols are the same as Figure 11.